Packing of Elastic Wires in Three-Dimensional Cavities

Master Thesis

Author(s):
Vetter, Roman (iD)

Publication date:
2011-05-02

Roman Vetter

Packing of Elastic Wires in Three-Dimensional Cavities

Master's Thesis

Group of Computational Physics for Engineering Materials (comphys)
Institute for Building Materials (IfB)
Swiss Federal Institute of Technology (ETH) Zurich
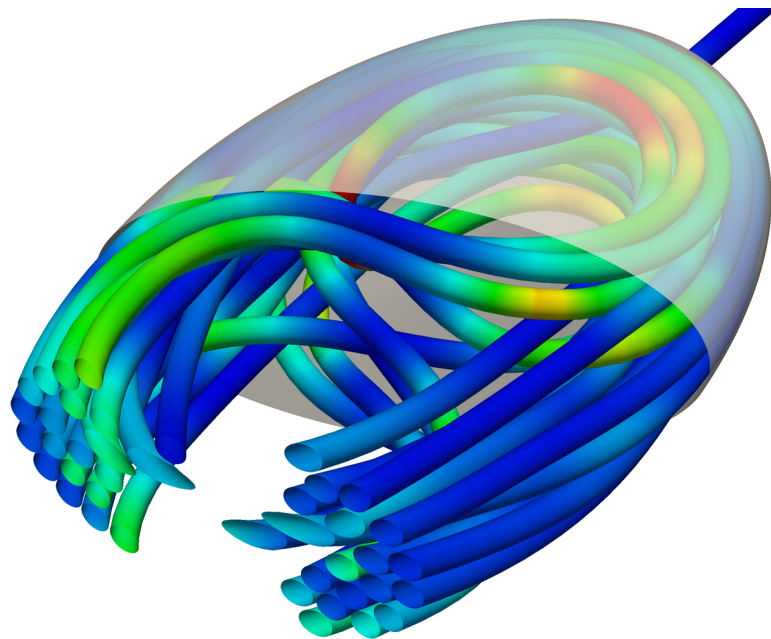
Supervisor

Prof. Dr. Hans J. Herrmann

Advisors

Dr. Falk K. Wittel
Dr. Norbert Stoop

May 2, 2011

ABSTRACT

A finite element program is developed to simulate the packing and coiling of elastic wires in three-dimensional cavities. The wire is modelled with third order beam theory and embedded into a corotational formulation to capture the geometric nonlinearity resulting from large rotations and deformations. Wire-wire contacts are found efficiently with the aid of linked cell lists. The hyperbolic equations of motion are integrated in time using two different integration methods from the Newmark family: Implicitly with a Newton-Raphson iterative solver combined with a line search algorithm, and explicitly with an adaptive-timestep predictor-corrector scheme. The two methods reveal fundamentally different suitability for the problem of strongly self-interacting finite elements as they are encountered in densely packed cavities, in particular, the implicit scheme is unable to access the dense regime due to convergence failure at multiple self-contacts. The computational performance of the two methods is compared, and their parallelization is discussed. With the explicit solver, some aspects of the packing of frictionless elastic wires with zero intrinisic curvature in hard ellipsoidal cavities are studied as a first step toward arbitrary or deformable cavities, i.e. away from the spherical symmetry investigated in recent studies.

ACKNOWLEDGEMENT

Contents

List of Figures

List of Symbols

The following is a selected list of the most significant and frequently recurring symbols in this thesis.

Uppercase scalars:

Lowercase scalars:

Greek scalars:

Matrices:

Vectors:

Many symbols can carry a subscript like $\mathbf{X}_n$ or $\mathbf{X}_e$, in which case the submatrix of $\mathbf{X}$ (or subvector or scalar) belonging to node n or element e is meant. Symbols carrying a hat like $\hat{\theta}$ refer to quantities w.r.t. the corotated local element frame, whereas quantities without a hat (θ) are generally expressed in the fixed global cartesian frame.

1. Introduction

Saccular aneurysms are permanent, roughly spherical bulges in mainly arterial blood vessels. The surgical treatment of saccular aneurysms has been subject to quite some technological progress in the past two decades. In 1991, a new minimally invasive technique called *endovascular coiling* has been successfully applied for the first time by Guglielmi and co-workers [1]. To reduce internal blood circulation leading to further increase in size of the aneurysm and eventual rupturing of the vascular walls, the aneurysm is occluded by inserting a detachable platinum coil through a catheter. A high packing density of the coiled wire is desired as it leads to better long-term stability of the embolization [2]. This is one reason among many why the morphological packing and coiling behavior of wires in three-dimensional cavities depending on material properties and geometry has attracted increasing interest in recent research.

In the past few years and in a more physics-oriented context, the crumpling of thin wires has been studied in two dimensions experimentally by Donato, Gomes and co-workers [3–7] followed by numerical simulations by Stoop *et al.* [8]. It wasn't until very recently that experiments were extended to three dimensions [9, 10]. A numerical study of the three-dimensional case again by Stoop *et al.* [10] is now unveiling a rich range of interesting morphological phases largely dependent on geometry and twist rather than intrinsic curvature, friction or energy scales of the wire.

The above-mentioned existing studies of crumpled wires have one particular aspect in common: they all use hard, spherical or cylindrical cavities. Material nonlinearities of either the wire or the cavity, as well as deformation of the latter, are not adressed. For a realistic simulation of endovascular coiling, existing models need extensions in this regard. In the present work, a reimplementation from scratch using finite elements is presented. The long-term goal of this effort is the development of a fully integrated finite element program capable of capturing both wire and cavity deformations, material nonlinearities, plasticity and friction. The wire is modelled with third order beam theory and embedded into a corotational formulation to capture the geometric nonlinearity resulting from large rotations and deformations. The hyperbolic equations of motion are integrated in time using two different integration methods from the Newmark family [11]: Implicitly with a Newton-Raphson iterative solver combined with a line search algorithm, and explicitly with an adaptive-timestep predictor-corrector scheme. The two methods are compared w.r.t. suitability for densely packed systems and computational performance. With the explicit solver, some aspects of the packing of frictionless elastic wires with zero intrinisic curvature in hard ellipsoidal cavities are studied as a first step away from strictly spherical confinement.

2. Finite Element Model

In this chapter, the finite element description is presented, which is deployed for modelling the bending deformation of elastic rods, their self-interaction, and spatial confinement inside a hard ellipsoidal cavity. The wire is represented in terms of a one-dimensional regular mesh with N elements $\{e\}$, i.e. $N+1$ nodes $\{n\}$. The mesh has a fixed position $\mathbf{x} \in \mathbb{R}^{3(N+1)}$ parallel to the global x-axis in the simulations. However, with respect to potential future adaptive mesh refinement and coarsening or material nonlinearities, the mesh spacing h is generalized to element-dependant values h_e throughout the theoretical considerations and implementation. Each mesh node is populated by six degrees of freedom (*DoFs*): three cartesian displacements u_n, v_n, w_n in x-, y- and z-direction, respectively, and three Euler angles φ_n, θ_n, ψ_n for rotations around these respective axes, giving each node an orientation in space.

Eventually, the motion of the wire will be described by the nonlinear system of hyperbolic differential equations

$$\mathbf{M}\ddot{\mathbf{u}} + \mathbf{C}\dot{\mathbf{u}} + \mathbf{K}(\mathbf{u})\mathbf{u} = \mathbf{f}_{\text{ext}}(\mathbf{u}). \tag{2.1}$$

Here, $\mathbf{M}$ is the wire's *mass matrix*, $\mathbf{C}$ is a *damping matrix* and $\mathbf{K}(\mathbf{u})$ represents the solution-dependent "nonlinear" *stiffness matrix*. Each of these matrices is a member of $\mathbb{R}^{6(N+1)\times 6(N+1)}$. The global solution vector $\mathbf{u} = \mathbf{u}(t) \in \mathbb{R}^{6(N+1)}$ contains the six DoFs for each node at time t. All external forces and torques acting on the wire at time t enter the solution-dependent right-hand side vector $\mathbf{f}_{\text{ext}}(\mathbf{u})$. This includes self-contact forces between disjoint wire elements, forces due to penetration of the cavity, and the boundary force responsible for pushing the wire into the cavity. The left-hand side is often termed *internal force*, i.e. (2.1) balances internal and external forces.

As is customary in finite element formulations, all matrices and vectors in (2.1) are assembled from their element or nodal contributions. That is,

$$\mathbf{K} = \bigoplus_e \mathbf{K}_e, \tag{2.2}$$

where the *element stiffness matrix* $\mathbf{K}_e \in \mathbb{R}^{12\times 12}$ describes the stiffness of element e on its 12 DoFs, and $\bigoplus$ denotes the cumulative submatrix assembly operation following a prescribed local-to-global element DoF mapping. The corresponding formalism applies to all other terms in (2.1), e.g., the overall solution vector $\mathbf{u}$ is built up from nodal contributions

$$\mathbf{u}_n = [u_n, v_n, w_n, \varphi_n, \theta_n, \psi_n]^{\text{T}}, \in \mathbb{R}^6 \quad n = 0, 1, ..., N, \tag{2.3}$$

or equivalently, from element contributions

$$\mathbf{u}_e = [u_1, v_1, w_1, \varphi_1, \theta_1, \psi_1, u_2, v_2, w_2, \varphi_2, \theta_2, \psi_2]^{\text{T}}, \in \mathbb{R}^{12} \quad e = 1, 2, ..., N. \tag{2.4}$$

In (2.4), the subscript 1 refers to the element's left node n, while 2 refers to its right node $n+1$. This submatrix or subvector notation will be used extensively in the following. For instance, one may conveniently write

$$\mathbf{u} = [\mathbf{u}_0^{\mathrm{T}}, \mathbf{u}_1^{\mathrm{T}}, ..., \mathbf{u}_N^{\mathrm{T}}]^{\mathrm{T}}. \tag{2.5}$$

2.1. Direct Mass Lumping

The first in a series of approximations to be conducted is simplifying $\mathbf{M}$ and $\mathbf{C}$ in (2.1) by means of *direct mass lumping* [12, 13]. The masses of each cylindrical element are effectively distributed to its two end nodes in equal parts:

$$m_e = h_e A\rho \qquad \longrightarrow \qquad m_n = \frac{h_n + h_{n+1}}{2} A\rho \tag{2.6}$$

where $A = \pi r^2$ is the area cross section of the tubular wire and ρ its mass density. The nodal moments of inertia that enter the mass matrix are approximated in a similar fashion. The nodal point masses m_n are simply uniformly distributed to balls of the same radius as the wire, resulting in

$$J_n = \frac{2}{5} m_n r^2 = \frac{h_n + h_{n+1}}{5} \pi r^4 \rho. \tag{2.7}$$

The procedure is visualized in Figure 2.1.
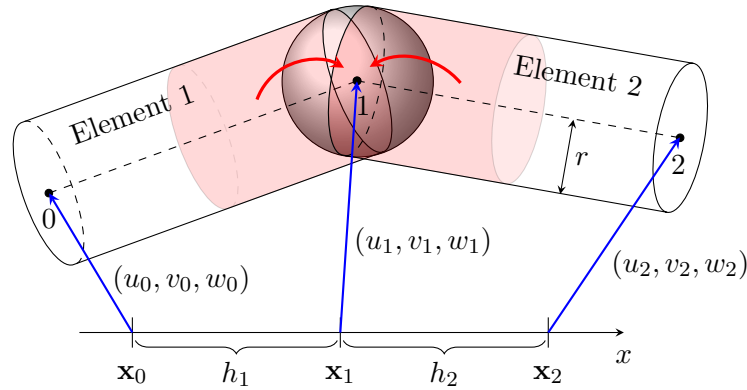
Figure 2.1.: Lumping of masses and moments of inertia to the nodes. Half of the mass and moment of inertia of each element is assigned to each node (red). The masses are concentrated in points, while for the calculation of the nodal moment of inertia J, they are uniformly distributed in a sphere of radius r.

Direct mass lumping leads to a diagonalization of $\mathbf{M}$, which is then called *diagonally lumped mass matrix*. The nodal contribution to $\mathbf{M}$ is

$$\mathbf{M}_n = \text{diag}(m_n, m_n, m_n, J_n, J_n, J_n). \tag{2.8}$$

This approach proves particularly useful for explicit time integration (cf. Section 3.2), where a matrix inversion for the computation of nodal accelerations

$$\ddot{\mathbf{u}} = \mathbf{M}^{-1}\big(\mathbf{f}_{\text{ext}}(\mathbf{u}) - \mathbf{C}\dot{\mathbf{u}} - \mathbf{K}(\mathbf{u})\mathbf{u}\big) \tag{2.9}$$

reduces to a simple componentwise vector multiplication. Moreover, the total kinetic energy of the wire can now be written as

$$
\begin{aligned}
E_{\text{k}} &= \frac{1}{2}\dot{\mathbf{u}}^{\text{T}}\mathbf{M}\dot{\mathbf{u}} = \frac{1}{2}\sum_n \dot{\mathbf{u}}_n^{\text{T}}\mathbf{M}_n\dot{\mathbf{u}}_n \\
&= \frac{1}{2}\sum_n \left\{ m_n\left(\dot{u}_n^2 + \dot{v}_n^2 + \dot{w}_n^2\right) + J_n\left(\dot{\varphi}_n^2 + \dot{\theta}_n^2 + \dot{\psi}_n^2\right)\right\}.
\end{aligned}
\tag{2.10}
$$

In many situations, Rayleigh damping of the form

$$\mathbf{C} = c_1\mathbf{M} + c_2\mathbf{K}, \qquad c_1, c_2 \geq 0 \tag{2.11}$$

serves as an expedient damping model, especially for irregular meshes. However, in this thesis the damping matrix is simply lumped to $\mathbf{C} = c_{\text{v}}\mathbb{1}_{6(N+1)}$, where $c_{\text{v}} \geq 0$ is a scalar viscous damping coefficient acting on all translational and angular velocities equally. This will be sufficient to effectively control vibrational instability in a first step.

The rest of this chapter is devoted to the construction of the stiffness matrix $\mathbf{K}$ and external forces $\mathbf{f}_{\text{ext}}$. For implicit integration in time, the need to also provide the Jacobian matrix for these will come across.

2.2. Linear Two-Dimensional Beam Theory

The deformation of the tubular wire is modelled by means of well-established beam theory. The most common beam theories differ in the treatment or neglect of transverse shear and transverse normal effects [14]. The Euler-Bernoulli beam theory (EBT), as the most elementary version, completely neglects these. The Timoshenko beam theory (TBT) [15,16] introduces a constant shear strain, resulting in a linear shear stress profile. Timoshenko finite elements are known to suffer from a problem called *shear locking* [17,18], which is an overstiff reaction to thinness of the beam due to inconsistent interpolation of the translational and rotational degrees of freedom. In 1997, Reddy proposed a third-order beam theory that includes the real quadratic shear stress distribution [14,19]. In a simplified version, hereafter referred to as RBT, where the differential equations are reduced from sixth to forth order, his theory beautifully generalizes both EBT and TBT at once, resulting in a "unified" theory that completely alleviates shear locking without complicating the stiffness matrix. For that reason, RBT is deployed here for the bending deformation of the rods.

For brevity, the derivation of a beam finite element from the continuum equations is skipped here. A condensed overview can be found in Ref. [19]. Here only the parts relevant for implementation are reiterated.

Common beam theories are usually devised in two dimensions and in the linear limit, i.e. for small deflections and rotations. Reddy's unified element stiffness matrix for a small bending deflection $w(x)$ in the xy-plane, assuming constant beam material and geometry, reads [19]

$$
\mathbf{K}_{e,\mathrm{2D}} =
\begin{bmatrix}
k_w & -k_{w\theta} & -k_w & -k_{w\theta} \\
    & k_\theta & k_{w\theta} & k_{\theta\theta} \\
    &   & k_w & k_{w\theta} \\
\text{symm.} & & & k_\theta
\end{bmatrix}
\tag{2.12}
$$

with entries

$$
k_w = \frac{12EI_{yy}}{\mu h_e^3}, \qquad
k_\theta = \frac{4EI_{yy}}{\mu h_e}\lambda, \qquad
k_{w\theta} = \frac{6EI_{yy}}{\mu h_e^2}, \qquad
k_{\theta\theta} = \frac{2EI_{yy}}{\mu h_e}\xi, \qquad (2.13)
$$

$$
\mu = 1 + 12\Omega, \qquad \lambda = 1 + 3\Omega, \qquad \xi = 1 - 6\Omega. \tag{2.14}
$$

Ω is the parameter determining the order of the theory:

$$
\Omega =
\begin{cases}
0 & \text{for EBT} \\
\frac{\hat{D}_{xx}}{\hat{A}_{xz}h_e^2} & \text{for RBT}
\end{cases}.
\tag{2.15}
$$

For RBT, the stiffness coefficients

$$
\begin{aligned}
\hat{D}_{xx} &= \bar{D}_{xx} - c_1\bar{F}_{xx}, & \hat{A}_{xz} &= \bar{A}_{xz} - c_2\bar{D}_{xz} \\
\bar{D}_{xx} &= E\big(I_{yy}^{(2)} - c_1 I_{yy}^{(4)}\big), & \bar{A}_{xz} &= G\big(A - c_2 I_{yy}^{(2)}\big) \\
\bar{F}_{xx} &= E\big(I_{yy}^{(4)} - c_1 I_{yy}^{(6)}\big), & \bar{D}_{xz} &= G\big(I_{yy}^{(2)} - c_2 I_{yy}^{(4)}\big),
\end{aligned}
\tag{2.16}
$$

are needed, with

$$
c_1 = \frac{1}{3r^2}, \qquad c_2 = 3c_1 = \frac{1}{r^2}, \tag{2.17}
$$

where r is the half thickness of the beam, i.e. the cross section radius for a tubular wire. E denotes the Young's modulus of elasticity of the wire, and G its shear modulus. I will use the linear elasticity ansatz

$$
G = \frac{E}{2(1+\nu)}, \tag{2.18}
$$

where ν is the Poisson ratio. $I_{yy}^{(i)}$ is the i-th moment of inertia of the wire about the y-axis, and calculates as

$$
I_{yy}^{(i)} = \int_A z^i \, \mathrm{d}A. \tag{2.19}
$$

With (2.12), the equilibrium internal element forces are calculated as

$$
\mathbf{f}_{\mathrm{int},e} = \mathbf{K}_{e,\mathrm{2D}} \, \mathbf{u}_{e,\mathrm{2D}}, \tag{2.20}
$$

where $\mathbf{u}_{e,\mathrm{2D}} = [w1, \theta_1, w_2, \theta_2]^{\mathrm{T}}$ holds the four DoFs of a two-dimensional element.

This element stiffness matrix for a 2D beam holds only for cubic Hermite shape functions, which have been analytically integrated over the element $[0, h_e]$ in (2.12). There is no more need for numerical integration using quadrature rules. Cubic Hermite splines are C^1-shape functions defined on the standard unit element with natural coordinate $0 \leq \xi = \frac{x}{h_e} \leq 1$ by [20]

$$
\begin{aligned}
H_1(\xi) &= (2\xi + 1)(\xi - 1)^2 \\
H_2(\xi) &= -\xi(\xi - 1)^2 \\
H_3(\xi) &= -\xi^2(2\xi - 3) \\
H_4(\xi) &= -\xi^2(\xi - 1)
\end{aligned}
\tag{2.21}
$$

These are shown in Figure 2.2. The displacement field w is then interpolated in the usual way:

$$
w(x) = \sum_{i=1}^{4} (\mathbf{u}_e)_i \, H_i(x/h_e), \quad 0 \leq x = \xi h_e \leq h_e.
\tag{2.22}
$$
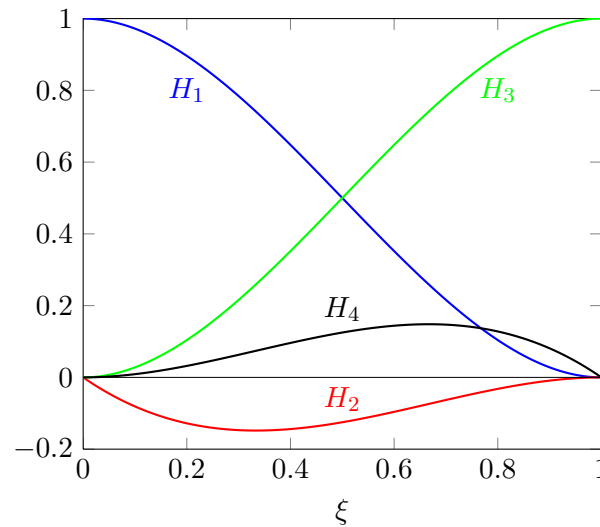
Figure 2.2.: The four cubic Hermite shape functions on the standard element.

2.3. Linear Tree-Dimensional Beam Theory

The extension to three dimensions is straightforward. The deflection field w in the xy-plane is complemented by another one, v, in the xz-plane. Additionally, a longitudinal displacement u and a twist angle φ are introduced, both of which are modelled with Hooke's law. These four fields are completely independent in the linear theory by construction, which is yet another approximation. This implies for instance that vanishing mixed-bending Cauchy stresses

$$\sigma_{yz} = \sigma_{zy} = 0 \tag{2.23}$$

are assumed. However, in Section 2.4, the embedding of the beam elements into a corotational formulation will turn the theory nonlinear and thereby couple the fields to some degree.

Special attention needs to be paid to the sign convention in 3D. For consistency with literature and other common available FEM software, the signs of H_2 and H_4 in (2.21) are flipped for the second bending plane such that the "slopes" ϕ_n are equally oriented as the conventinal Euler angles. Consequently, the stiffness matrix entries coupling v_1 and v_2 with ψ_1 and ψ_2 must flip their signs as well. Let's order the 12 DoFs of an element as in (2.4). The full 3D element stiffness matrix then reads

$$\mathbf{K}_{e,\mathrm{3D}} = \begin{bmatrix} k_u & 0 & 0 & 0 & 0 & 0 & -k_u & 0 & 0 & 0 & 0 & 0 \\ & k_v & 0 & 0 & 0 & k_{v\psi} & 0 & -k_v & 0 & 0 & 0 & k_{v\psi} \\ & & k_w & 0 & -k_{w\theta} & 0 & 0 & 0 & -k_w & 0 & -k_{w\theta} & 0 \\ & & & k_\varphi & 0 & 0 & 0 & 0 & 0 & -k_\varphi & 0 & 0 \\ & & & & k_\theta & 0 & 0 & 0 & -k_{w\theta} & 0 & k_{\theta\theta} & 0 \\ & & & & & k_\psi & 0 & k_{v\psi} & 0 & 0 & 0 & k_{\psi\psi} \\ & & & & & & k_u & 0 & 0 & 0 & 0 & 0 \\ & & & & & & & k_v & 0 & 0 & 0 & -k_{v\psi} \\ & & \text{symm.} & & & & & & k_w & 0 & k_{w\theta} & 0 \\ & & & & & & & & & k_\varphi & 0 & 0 \\ & & & & & & & & & & k_\theta & 0 \\ & & & & & & & & & & & k_\psi \end{bmatrix} \tag{2.24}$$

with components from (2.13) and

$$k_v = \frac{12EI_{zz}}{\mu h_e^3}, \qquad k_\psi = \frac{4EI_{zz}}{\mu h_e}\lambda, \qquad k_{v\psi} = \frac{6EI_{zz}}{\mu h_e^2}, \qquad k_{\psi\psi} = \frac{2EI_{zz}}{\mu h_e}\xi. \tag{2.25}$$

The longitudinal and torsional spring constants are given by

$$k_u = \frac{EA}{h_e}, \qquad k_\varphi = \frac{GJ}{h_e}, \tag{2.26}$$

where the polar moment of inertia $J = I_{yy} + I_{zz}$ by the perpendicular axis theorem. For a wire with circular profile A of radius r, one can write

$$I_{yy}^{(i)} = I_{zz}^{(i)} =: I^{(i)}, \tag{2.27}$$

which implies that

$$k_v = k_w, \quad k_\psi = k_\theta, \quad k_{v\psi} = k_{w\theta}, \quad k_{\theta\theta} = k_{\psi\psi}, \qquad (2.28)$$

and

$$A = \pi r^2, \quad I := I^{(2)} = \frac{\pi}{4} r^4, \quad I^{(4)} = \frac{\pi}{8} r^6, \quad I^{(6)} = \frac{5\pi}{64} r^8, \quad J = 2I = \frac{\pi}{2} r^4. \quad (2.29)$$

2.4. The Corotational Formulation

Linear beam theories are only valid in the small rotation and small deflection regime. Wires packed in cavities undergo large rotations and deflections, though. In order to comprise such deformations in a finite element simulation, geometric nonlinearity of the form $\mathbf{K} = \mathbf{K}(\mathbf{u})$ must be introduced to the theory. To this end, three prominent approaches have been developed, refined, mixed, and broadly applied over decades. The *total Lagrangian formulation* (TL) expresses the sought solution w.r.t. an initial configuration. The *updated Lagrangian formulation* (UL) can be shown to be effectively equivalent to TL [21], but making use of a different representation, where the nodal displacements and rotations are described incrementally, i.e. relative to the last known values. The *corotational formulation* (CR) introduces a local reference frame for each element that continuously moves and rotates with the element, within which the theory can be considered linear. CR has been acclaimed superiority over TL and UL in accuracy [22, 23], performance [24, 25], simplicity [26] and generality [25, 27], which is why it is utilized in the present work.

The corotational formulation appears to root in the work of Wempner [28], Belytschko & Hsieh [24] and Oran [29]. Based on the polar decomposition theorem, which states that any general motion can be expressed as the sum of a rigid body motion and a pure body deformation, it is designed for problems with large rotation and deformation, but small strains. The idea is to corotate and cotranslate a dedicated frame with each beam element, exactly passing through the nodes. The 12 global DoFs per element reduce to seven local ones when expressed w.r.t this corotated frame. In other words, each element is carefully reduced by its five rigid body DoFs, and the linear beam theory is then applied to the remaining seven DoFs, which are responsible for deformation in the local frame. In 1990, Crisfield [27, 30] was the first to provide a beam-theory-independent, three-dimensional CR formulation with consistent treatment of the tangent stiffness matrix, which is required for acceptable convergence in the Newton-Raphson solver. In the remainder of this section, a rough outline of Crisfield's method and its integration into the presented finite element model is given, adopting most of his original notation. This may appear somewhat brief for people unfamiliar with the subject. In fact, the CR formulation is one of the most complex and lengthy parts in the program. The reader is referred to Crisfield's literature for more details, especially on the assembly of the geometric stiffness matrix $\mathbf{K}_{\sigma,e}$, see below.

Let's denote the actual, global position of a node n in space by the sum of its mesh coordinates and displacement,

$$\mathbf{p}_n = \mathbf{x}_n + [u_n, v_n, w_n]^{\mathrm{T}} \in \mathbb{R}^3. \tag{2.30}$$

Each beam element e is assigned a unit triad $\mathbf{E}_e = [\mathbf{e}_1, \mathbf{e}_2, \mathbf{e}_3] \in \mathbb{R}^{3\times3}$, called the *corotated frame*, in such a way that it represents the orientation of e, in particular, $\mathbf{e}_1$ is colinear to the line connecting the two nodes,

$$\mathbf{e}_1 = \frac{\mathbf{p}_2 - \mathbf{p}_1}{|\mathbf{p}_2 - \mathbf{p}_1|}. \tag{2.31}$$

The global element Dofs $\mathbf{u}_e$ are now expressed w.r.t. $\mathbf{E}_e$. All variables carrying a hat refer to this local element frame in the following. By construction, it holds that

$$\hat{v}_1 = \hat{v}_2 = \hat{w}_1 = \hat{w}_2 = 0. \tag{2.32}$$

Additionally, the longitudinal displacement variables u_1, u_2 can be reduced to a single longitudinal spring deflection

$$\hat{u}_e = |\mathbf{p}_2 - \mathbf{p}_1| - h_e. \tag{2.33}$$

Each node is further assigned another unit triad, call it $\mathbf{T}_e = [\mathbf{t}_1, \mathbf{t}_2, \mathbf{t}_3]$ for node 1 and $\mathbf{V}_e = [\mathbf{v}_1, \mathbf{v}_2, \mathbf{v}_3]$ for node 2 when element e is considered. These triads represent the nodal orientations, that were previously identified by φ_1, θ_1, ψ_1 and φ_2, θ_2, ψ_2 in the linear theory. It turns out that if these three triads are defined and updated properly, one can compute the six rotational DoFs w.r.t. $\mathbf{E}_e$ as

$$\begin{aligned}
\hat{\varphi}_1 &= \sin^{-1}\left(\frac{\mathbf{t}_2^{\mathrm{T}}\mathbf{e}_3 - \mathbf{t}_3^{\mathrm{T}}\mathbf{e}_2}{2}\right) - \hat{\varphi}_1^0, & \hat{\varphi}_2 &= \sin^{-1}\left(\frac{\mathbf{v}_2^{\mathrm{T}}\mathbf{e}_3 - \mathbf{v}_3^{\mathrm{T}}\mathbf{e}_2}{2}\right) - \hat{\varphi}_2^0, \\
\hat{\theta}_1 &= \sin^{-1}\left(\frac{\mathbf{e}_2^{\mathrm{T}}\mathbf{t}_1 - \mathbf{t}_2^{\mathrm{T}}\mathbf{e}_1}{2}\right) - \hat{\theta}_1^0, & \hat{\theta}_2 &= \sin^{-1}\left(\frac{\mathbf{e}_2^{\mathrm{T}}\mathbf{v}_1 - \mathbf{v}_2^{\mathrm{T}}\mathbf{e}_1}{2}\right) - \hat{\theta}_2^0, \\
\hat{\psi}_1 &= \sin^{-1}\left(\frac{\mathbf{e}_3^{\mathrm{T}}\mathbf{t}_1 - \mathbf{t}_3^{\mathrm{T}}\mathbf{e}_1}{2}\right) - \hat{\psi}_1^0, & \hat{\psi}_2 &= \sin^{-1}\left(\frac{\mathbf{e}_3^{\mathrm{T}}\mathbf{v}_1 - \mathbf{v}_3^{\mathrm{T}}\mathbf{e}_1}{2}\right) - \hat{\psi}_2^0,
\end{aligned} \tag{2.34}$$

where $\hat{\varphi}^0, \hat{\theta}^0, \hat{\psi}^0$ allow to give the beam an intrinsic equilibrium curvature.
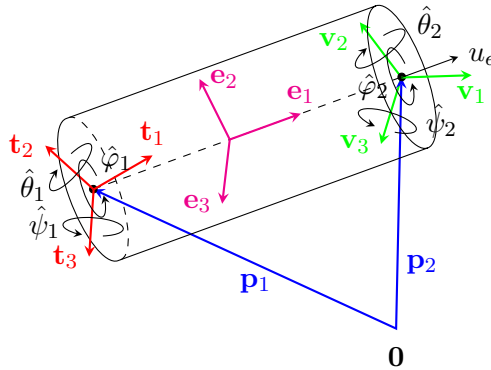

Figure 2.3.: Visualization of the corotated wire element: The nodal triads $\mathbf{T}_e$ (red) and $\mathbf{V}_e$ (green), the corotated element frame $\mathbf{E}_e$ (magenta) and the seven local DoFs.

This defines the seven local deformation DoFs $\hat{\mathbf{u}}_e = [\hat{\varphi}_1, \hat{\theta}_1, \hat{\psi}_1, \hat{u}_e, \hat{\varphi}_2, \hat{\theta}_2, \hat{\psi}_2]^\mathrm{T}$ from which the rigid body motion has been completely detached. They are illustrated together with the triads in Figure 2.3. The 7×7 element stiffness matrix acting on these local DoFs is now easily devised from any linear beam theory with two nodes per element and six DoFs per node, three translational and three rotational. All that needs to be done for RBT is eliminating the stiffness coefficients involving bending deflection (v, w), as that vanishes in the corotated frame, and condensing the two rows/columns for the longitudinal stiffness into one. The reduced corotational RBT stiffness matrix thus simply reads

$$
\hat{\mathbf{K}}_e =
\begin{bmatrix}
k_\varphi & 0 & 0 & 0 & -k_\varphi & 0 & 0 \\
 & k_\theta & 0 & 0 & 0 & k_{\theta\theta} & 0 \\
 & & k_\psi & 0 & 0 & 0 & k_{\psi\psi} \\
 & & & k_u & 0 & 0 & 0 \\
 & & & & k_\varphi & 0 & 0 \\
 & \text{symm.} & & & & k_\theta & 0 \\
 & & & & & & k_\psi
\end{bmatrix}
\tag{2.35}
$$

with coefficients from (2.13), (2.25) and (2.26). The key observation is now that $\hat{\mathbf{K}}_e$ can be transformed into the desired 12×12 "nonlinear" global element stiffness matrix $\mathbf{K}_e(\mathbf{u}_e)$ via a solution-dependent global-to-local transformation matrix $\mathbf{F}_e(\mathbf{u}_e) \in \mathbb{R}^{7 \times 12}$:

$$
\mathbf{K}_e(\mathbf{u}_e) = \mathbf{F}_e^\mathrm{T}(\mathbf{u}_e) \hat{\mathbf{K}}_e \mathbf{F}_e(\mathbf{u}_e).
\tag{2.36}
$$

This is where geometric nonlinearity enters the equations of motion. Equivalently, one can write

$$
\mathbf{f}_{\mathrm{int},e}(\mathbf{u}_e) = \mathbf{F}_e^\mathrm{T}(\mathbf{u}_e) \hat{\mathbf{K}}_e \hat{\mathbf{u}}_e
\tag{2.37}
$$

for the internal forces in static equilibrium. The construction of $\mathbf{F}_e$ is done row-wise and turns out to be somewhat lengthy matrix calculus involving the three triads $\mathbf{E}_e$, $\mathbf{T}_e$ and $\mathbf{V}_e$. The details are omitted here, but note that for the undeformed initial state $\mathbf{u} \equiv \mathbf{0}$, the transformation matrix is exactly such that $\mathbf{K}_e(\mathbf{u}_e)$ is identical to the linear case from (2.24), $\mathbf{K}_{e,3\mathrm{D}}$.

For an initially straight beam colinear to the x-axis, the nodal triads are just identity matrices. When the equilibrium equations (2.1) are integrated in time, the wire deforms and the nodal triads need to be updated in accordance to the nodal rotational degrees of freedom. In order to avoid the singularities occurring in an Eulerian representation of large rotations, unit quaternions are used instead. Thus, in a practical implementation, the three angles φ_n, θ_n, ψ_n are replaced by four quaternion components

$$
\mathbf{q}_n =
\begin{bmatrix}
q_0 \\
q_1 \\
q_2 \\
q_3
\end{bmatrix}
=
\begin{bmatrix}
\cos(\varphi_n/2)\cos(\theta_n/2)\cos(\psi_n/2) + \sin(\varphi_n/2)\sin(\theta_n/2)\sin(\psi_n/2) \\
\sin(\varphi_n/2)\cos(\theta_n/2)\cos(\psi_n/2) - \cos(\varphi_n/2)\sin(\theta_n/2)\sin(\psi_n/2) \\
\cos(\varphi_n/2)\sin(\theta_n/2)\cos(\psi_n/2) + \sin(\varphi_n/2)\cos(\theta_n/2)\sin(\psi_n/2) \\
\cos(\varphi_n/2)\cos(\theta_n/2)\sin(\psi_n/2) - \sin(\varphi_n/2)\sin(\theta_n/2)\cos(\psi_n/2)
\end{bmatrix}.
\tag{2.38}
$$

The nodal triad $\mathbf{T}_n$ can be calculated from the nodal unit quaternion as

$$\mathbf{T}_n = \begin{bmatrix} q_0^2 + q_1^2 - q_2^2 - q_3^2 & 2(q_1q_2 - q_0q_3) & 2(q_0q_2 + q_1q_3) \\ 2(q_1q_2 + q_0q_3) & q_0^2 - q_1^2 + q_2^2 - q_3^2 & 2(q_2q_3 - q_0q_1) \\ 2(q_1q_3 - q_0q_2) & 2(q_0q_1 + q_2q_3) & q_0^2 - q_1^2 - q_2^2 + q_3^2 \end{bmatrix}. \tag{2.39}$$

The incremental update of the nodal quaternions in time is realized by quaternion multiplication. The nodal quaternions are normalized on a regular basis to preserve their unit length. The missing vectors $\mathbf{e}_2$ and $\mathbf{e}_3$ are detemined via a fourth triad $\bar{\mathbf{R}}_e = [\mathbf{r}_1, \mathbf{r}_2, \mathbf{r}_3]^{\mathrm{T}}$, which is obtained from $\mathbf{T}_e$ and $\mathbf{V}_e$ as a nonlinear average between the two. Again, the details are skipped, but are readily available in Refs. [27, 30].

The most significant part in Crisfield's work is the derivation of a tangent stiffness matrix

$$\mathbf{K}_{\mathrm{t},e}(\mathbf{u}_e) = \frac{\partial}{\partial \mathbf{u_e}} \mathbf{K}_e(\mathbf{u}_e) \mathbf{u}_e \tag{2.40}$$

that is consistent with the rest of the formalism, which enables an efficient application of the Newton-Raphson method for implicit integration of the equations of motion (2.1) in time. This is a highly non-trivial task and requires even more linear algebra than the assembly of $\mathbf{F}_e$. As will be shown in Section 4.3, it is also an expensive one in terms of required CPU time. By the product rule of differential calculus, it can be written as

$$\mathbf{K}_{\mathrm{t},e}(\mathbf{u}_e) = \mathbf{K}_e(\mathbf{u}_e) + \mathbf{K}_{\sigma,e}(\mathbf{u}_e) \tag{2.41}$$

with $\mathbf{K}_e$ from (2.36). The so-called *geometric stiffness matrix* $\mathbf{K}_{\sigma,e}$ is a lengthy sum of submatrices expressed in terms of the four triads, the internal forces $\mathbf{f}_{\mathrm{int},e}$, the local DoFs $\hat{\mathbf{u}}_e$ and the corotational transformation matrix $\mathbf{F}_e$.

In summary, the CR formulation is a very elegant, yet quite intricate method to introduce geometric nonlinearity to the system. Its beauty lies in the fact that the linear RBT can be made nonlinear without modification of the original concept of integrating over the cubic Hermite splines analytically. This is part of the reason why CR usually beats Lagrangian approaches in efficiency and accuracy. If the equations of motion are integrated with an explicit scheme, no Jacobian is needed and thus the most complex part of the implementation, the assembly of $\mathbf{K}_{\sigma,e}$, even drops out.

2.5. Strain Energy

In this section, some formulas for the most significant terms in the total strain energy of the discretized wire are briefly disclosed. The potential bending energy of a two-dimensional beam $\mathbf{p}: [0, L] \to \mathbb{R}^2$ is given by the integrated squared curvature

$$U_{\mathrm{b}} = \frac{1}{2} EI \int_0^L \left(\frac{\mathrm{d}^2 \mathbf{p}(s)}{\mathrm{d}s^2} \right)^2 \mathrm{d}s \tag{2.42}$$

which is linearized to

$$U_{\mathrm{b}} = \frac{1}{2} EI \int_0^L \left(\frac{\mathrm{d}^2 w}{\mathrm{d}x^2} \right)^2 \mathrm{d}x \tag{2.43}$$

for small displacements in the linear Euler-Bernoulli theory. This discretizes to the finite elements via (2.22) as

$$\begin{aligned}
U_{\mathrm{b}} &= \frac{1}{2} EI \sum_e \int_0^{h_e} \left(\sum_{i=1}^4 (\mathbf{u}_e)_i \frac{\mathrm{d}^2 H_i}{\mathrm{d}\xi^2}(x/h_e) \right)^2 h_e^2 \, \mathrm{d}x \\
&= \frac{1}{2} EI \sum_e \frac{4}{h_e} \left(3 \left\{ \Delta w_e^2 + \Delta w_e (\theta_1 + \theta_2) + \theta_1 \theta_2 \right\} + \Delta \theta_e^2 \right),
\end{aligned} \tag{2.44}$$

where $\Delta w_e = w_2 - w_1$ and $\Delta \theta_e = \theta_2 - \theta_1$, and the subscripts 1 and 2 again refer to the left and right node for each element e. In the corotated frame, one has $\hat{w}_1 = \hat{w}_2 = 0$ by construction for each element, and thus the expression simplifies to

$$U_{\mathrm{b}} = \frac{1}{2} EI \sum_e \frac{4}{h_e} \left(\hat{\theta}_1^2 + \hat{\theta}_2^2 + \hat{\theta}_1 \hat{\theta}_2 \right). \tag{2.45}$$

Finally, bending in the second spatial dimension is included to arrive at the full three-dimensional nonlinear finite element formula

$$U_{\mathrm{b}} = \frac{1}{2} EI \sum_e \frac{4}{h_e} \left(\hat{\theta}_1^2 + \hat{\theta}_2^2 + \hat{\theta}_1 \hat{\theta}_2 + \hat{\psi}_1^2 + \hat{\psi}_2^2 + \hat{\psi}_1 \hat{\psi}_2 \right). \tag{2.46}$$

It should be noted that the above derivation is only exact for EBT, where the second-order DoFs represent the actual slope at the element endpoints,

$$\theta_n = -\frac{\mathrm{d}w_n}{\mathrm{d}x} \qquad \text{and} \qquad \psi_n = \frac{\mathrm{d}v_n}{\mathrm{d}x}, \tag{2.47}$$

and the beam center line can be interpolated using the Hermite basis functions (2.21,2.22). This doesn't hold for the simplified third-order theory, where the second-order DoFs are "abused" for the shear strain approximation. In Ref. [31], Reddy provides the full strain energy in variational form for the third order theory, which is impossible to retrieve in simplified RBT finite elements. However, the CR-EBT formula (2.46) may be used as a close approximation of the pure bending contribution to the strain energy also for CR-RBT.

The axial elastic strain energy of a linear beam is straightforwardly obtained from Hooke's law:

$$U_{\mathrm{s}} = \frac{1}{2} E A \int_0^L \left(\frac{\mathrm{d}u}{\mathrm{d}x} \right)^2 \, \mathrm{d}x \tag{2.48}$$

with finite element approximation

$$U_{\mathrm{s}} = \frac{1}{2} E A \sum_e \frac{\Delta u_e^2}{h_{\mathrm{e}}}, \tag{2.49}$$

where $\Delta u_e = u_2 - u_1$ as usual. Since Δu_e appears exactly as $\hat{u}_{\mathrm{e}}$ in the calculation of the corotational transformation according to (2.33), one can easily calculate the axial elastic energy as

$$U_{\mathrm{s}} = \frac{1}{2} E A \sum_e \frac{\hat{u}_{\mathrm{e}}^2}{h_{\mathrm{e}}} \tag{2.50}$$

in the corotated frames. Analogously, the torsional potential energy is given by

$$U_{\mathrm{t}} = \frac{1}{2} G J \sum_e \frac{\Delta \hat{\varphi}_e^2}{h_{\mathrm{e}}}, \qquad \Delta \hat{\varphi}_e = \hat{\varphi}_2 - \hat{\varphi}_1. \tag{2.51}$$

2.6. Cavity Contact

So far, no forces are present in the model that would prevent the wire from equilibrating toward a straight line. Spatial confinement is now introduced by a hard cavity with a small opening through which the wire is pushed inside. In the frictionless elastic limit, the interaction between wire and cavity happens through exchange of forces normal to the connecting interfaces. A Hertzian contact model [32] is perfectly sufficient for this purpose. Consider a fixed hard sphere with radius r_{cav} centered at the global origin, and assume that a mesh node n penetrates this cavity with *indentation depth*

$$D = |\mathbf{p}_n| - (r_{\mathrm{cav}} - r) > 0, \tag{2.52}$$

where $\mathbf{p}_n = [p_x, p_y, p_z]^{\mathrm{T}} = \mathbf{x}_n + [u_n, v_n, w_n]^{\mathrm{T}}$ is the effective nodal position in space, and r denotes the radius of the tubular wire as usual. In this case, an external force [33]

$$\mathbf{f}_{\mathrm{cav},n} = -\frac{\pi}{4} E^* \bar{h} D \, \mathbf{n}_n \in \mathbb{R}^3 \tag{2.53}$$

is applied to the three displacement DoFs of the node, where $\mathbf{n}_n = \mathbf{p}_n / |\mathbf{p}_n|$ is the normal vector pointing radially outwards, $\bar{h} = \frac{1}{2}(h_{n-1} + h_n)$ is the average standard length of the two incident rod elements, and E^* mixes the material parameters (E, ν) of the rod with those of the vacity, $(E_{\mathrm{cav}}, \nu_{\mathrm{cav}})$, according to

$$\frac{1}{E^*} = \frac{1 - \nu^2}{E} + \frac{1 - \nu_{\mathrm{cav}}^2}{E_{\mathrm{cav}}}. \tag{2.54}$$

The force (2.53) is that of a Hertzian contact between two parallel cylinders of length $\bar{h}$, which serves as a reasonable rough estimate for the real force exerted by a hard cavity to a cylinder. Quite conveniently, it is independent of r. An alternative model could consist of the Hertzian force between a sphere and a half-space, where the force not linearly proportional to D.

For implicit time integration, the Jacobian $\mathbf{J}_{\mathrm{cav},n} \in \mathbb{R}^{3 \times 3}$ of (2.53) is also needed. Using the standard rules of differential calculus, one easily finds

$$
\begin{aligned}
\mathbf{J}_{\mathrm{cav},n} &= \frac{\partial \mathbf{f}_{\mathrm{cav},n}}{\partial \mathbf{p}_n} \\
&= -\frac{\pi}{4} E^* \bar{h} \left(D \frac{\partial \mathbf{n}_n}{\partial \mathbf{p}_n} + \mathbf{n}_n \frac{\partial D}{\partial \mathbf{p}_n} \right) \\
&= -\frac{\pi}{4} E^* \bar{h} \left(\frac{D}{|\mathbf{p}_n|^2} \left\{ |\mathbf{p}_n| \frac{\partial \mathbf{p}_n}{\partial \mathbf{p}_n} - \mathbf{p}_n \frac{\partial |\mathbf{p}_n|}{\partial \mathbf{p}_n} \right\} + \mathbf{n}_n \mathbf{n}_n^{\mathrm{T}} \right) \\
&= -\frac{\pi}{4} E^* \bar{h} \frac{D}{|\mathbf{p}_n|} \left(\mathbb{1}_3 + \left\{ \frac{|\mathbf{p}_n|}{D} - 1 \right\} \mathbf{n}_n \mathbf{n}_n^{\mathrm{T}} \right),
\end{aligned}
\tag{2.55}
$$

which obviously requires $D > 0$. For $D \leq 0$ the nodal Jacobian is zero.

Next, this interaction is generalized to hard cavities of ellipsoidal shape, to break spherical symmetry as a first step toward flexible cavities. The calculation of the shortest distance between an exact ellipsoid and a point in space is known to be equivalent to the problem of finding the roots of a sixth order polynomial [34], for which no analytical solution is known. Thus, the indentation depth D required for the appropriate Hertzian contact force can only be found numerically, and so can the Jacobian, which would need to be determined for employing an implicit time integration scheme. Particularly concerning the Jacobian, this is very inconvenient and it can lead to convergence difficulties in the Newton-Raphson method. Instead, a closed-form approximation is developed here. Consider an ellipsoidal cavity given by

$$E(x,y,z) = \left(\frac{x}{a}\right)^2 + \left(\frac{y}{b}\right)^2 + \left(\frac{z}{c}\right)^2 = 1. \tag{2.56}$$

Since the Hertzian force (2.53) outgrows the internal forces of the wire even for small indentations D when compared to the length scales of the wire, its *magnitude* is far less important than its *direction*. Therefore, D can be legitimately approximated by

$$D \approx \left(\frac{a+b+c}{3} - r\right)\left(\sqrt{1+\Delta} - 1\right) \tag{2.57}$$

in which $\Delta > 0$ is a relative measure for the nodal penetration of an *effective* ellipsoid E_{eff}:

$$1 + \Delta = \left(\frac{p_x}{a-r}\right)^2 + \left(\frac{p_y}{b-r}\right)^2 + \left(\frac{p_z}{c-r}\right)^2 =: E_{\text{eff}}(\mathbf{p}_n). \tag{2.58}$$

A consistent approximation of the surface normal vector assuming that $\Delta \ll 1$ is found by the normalized gradient of the effective ellipsoid:

$$\mathbf{n}_n \approx \frac{\nabla E_{\text{eff}}(\mathbf{p}_n)}{|\nabla E_{\text{eff}}(\mathbf{p}_n)|} =: \frac{\tilde{\mathbf{p}}_n}{|\tilde{\mathbf{p}}_n|}. \tag{2.59}$$

The effective direction $\tilde{\mathbf{p}}_n$ can be compactly written as

$$\tilde{\mathbf{p}}_n = \mathbf{R}^{-2}\mathbf{p}_n \tag{2.60}$$

with a diagonal matrix

$$\mathbf{R} = \text{diag}(a-r, b-r, c-r) \in \mathbb{R}^{3\times3}. \tag{2.61}$$

The resulting Hertzian force is then found by inserting approximations (2.57) and (2.59) into (2.53). For the Jacobian, note that

$$\frac{\partial \mathbf{n}_n}{\partial \mathbf{p}_n} \approx \frac{1}{|\tilde{\mathbf{p}}_n|}\left(\mathbf{R}^{-2} - \frac{1}{|\tilde{\mathbf{p}}_n|^2}\tilde{\mathbf{p}}_n\tilde{\mathbf{p}}_n^{\text{T}}\mathbf{R}^{-2}\right) \tag{2.62}$$

and

$$\frac{\partial D}{\partial \mathbf{p}_n} \approx \frac{a+b+c}{3}\frac{1}{\sqrt{1+\Delta}}\tilde{\mathbf{p}}_n^{\text{T}}. \tag{2.63}$$

Inserting (2.62) and (2.63) in (2.55) yields the final expression

$$
\begin{aligned}
\mathbf{J}_{\text{cav},n} &= -\frac{\pi}{4} E^* \bar{h} \left(D \frac{\partial \mathbf{n}_n}{\partial \mathbf{p}_n} + \mathbf{n}_n \frac{\partial D}{\partial \mathbf{p}_n} \right) \\
&\approx -\frac{\pi}{4} E^* \bar{h} \frac{D}{|\tilde{\mathbf{p}}_n|} \left(\left\{ \mathbb{1}_3 - \frac{1}{|\tilde{\mathbf{p}}_n|^2} \tilde{\mathbf{p}}_n \tilde{\mathbf{p}}_n^{\mathrm{T}} \right\} \mathbf{R}^{-2} + \frac{1}{1 + \Delta - \sqrt{1 + \Delta}} \tilde{\mathbf{p}}_n \tilde{\mathbf{p}}_n^{\mathrm{T}} \right)
\end{aligned}
\tag{2.64}
$$

or zero if $\Delta \leq 0$. It's easy to verify that in the spherical limit $a = b = c = r_{\text{cav}}$, the Jacobians (2.55) and (2.64) are identical, because the approximations (2.62) and (2.63) become exact under spherical symmetry.

The impact of approximations (2.62) and (2.63) is twofold. First, the magnitude of the Hertzian contact force is subject to an error that grows with the disparity of a, b, c. Since the Hertzian contact model used here is itself only a crude approximation whose only purpose is to keep the wire inside the hard cavity, this has no negative consequence in practice. Second, the effective ellipsoid is slightly deformed. This defect is also minor for reasonbly balanced $a, b, c \gg r$ and vanishes for arbitrary a, b, c in the slender wire limit $r \to 0$.

This section is concluded with a note on pressure. The confined, packed wire imposes a bulk pressure on the cavity that can be measured by the sum of nodal forces divided by the surface area of the ellipsoid,

$$
P = \frac{1}{A_E} \sum_n |\mathbf{f}_{\text{cav},n}|.
\tag{2.65}
$$

The surface area of a general ellipsoid is not known in closed form either. A close estimate is given by a formula due to Thomson [35]:

$$
A_E \approx 4\pi \left(\frac{(ab)^p + (ac)^p + (bc)^p}{3} \right)^{1/p}, \qquad p = \frac{8}{5}.
\tag{2.66}
$$

2.7. Self-Contact

Just like the cavity contacts, the spatial self-interaction of the wire is modelled by exchange of Hertzian contact forces that enter the equations of motion (2.1) through the right-hand side $\mathbf{f}_{\mathrm{ext}}$, frictionless and fully elastic. Self-contact happens among pairs of wire elements (e_1, e_2), and the resulting forces act on the four involved nodes n_1, n_2 of element e_1 and n_3, n_4 of element e_2. For simplicity, all wire elements are treated as if they were exactly cylindrical in shape, which is an approximation given that cubic Hermite shape functions are used for the beam interpolation. In favor of a compact and general notation in the following mathematical outline, the four effective nodal positions are condensed into a single vector

$$\mathbf{p} = [\mathbf{p}_{n_1}, \mathbf{p}_{n_2}, \mathbf{p}_{n_3}, \mathbf{p}_{n_4}]^{\mathrm{T}} \in \mathbb{R}^{12}, \tag{2.67}$$

and the same ordering for the resulting force vector $\mathbf{f}_{\mathrm{self},e_1,e_2} \in \mathbb{R}^{12}$ and Jacobian $\mathbf{J}_{\mathrm{self},e_1,e_2} \in \mathbb{R}^{12 \times 12}$ is used in the following. For the moment being, let's assume that an interacting pair of elements has been found together with their closest points of approach on the center lines,

$$\begin{aligned}
\mathbf{c}_1 &= \mathbf{p}_{n_1} + s_1(\mathbf{p}_{n_2} - \mathbf{p}_{n_1}), \quad s_1 \in [0, 1], \\
\mathbf{c}_2 &= \mathbf{p}_{n_3} + s_2(\mathbf{p}_{n_4} - \mathbf{p}_{n_3}), \quad s_2 \in [0, 1].
\end{aligned} \tag{2.68}$$

A more detailed description of how to find such pairs and their contact parameters s_1, s_2 in practice is given in Section 3.4. Analogously to Section 2.6, the direction in which the forces are pointing is denoted by

$$\mathbf{n} = \frac{\Delta \mathbf{c}}{|\Delta \mathbf{c}|}, \qquad \Delta \mathbf{c} = \mathbf{c}_1 - \mathbf{c}_2, \tag{2.69}$$

and the depth of mutual indentation by

$$D = 2r - |\Delta \mathbf{c}| > 0. \tag{2.70}$$

Note that this actually treats the elements as spherocylinders, i.e. the cylindrical elements are capped at both ends by hemispheres. Given these circumstances, the Hertzian normal force for two cylinders with equal radii, intersecting each other perpendicularly, [33]

$$f_\perp = \frac{4}{3} E^* \sqrt{D^3 r}, \tag{2.71}$$

is applied and distributed to the four nodes by setting

$$\mathbf{f}_{\mathrm{self},e_1,e_2} = \frac{f_\perp}{2} \left(\boldsymbol{\omega} \otimes \mathbf{n} \right) \tag{2.72}$$

with linear nodal weights

$$\boldsymbol{\omega} = [1 - s_1, s_1, -(1 - s_2), -s_2]^{\mathrm{T}}. \tag{2.73}$$

Here, $\otimes$ denotes the Kronecker product. In words, the closer a node lies to the contact point between the two elements, the larger the force it experiences, pushing it away from the other element. This linear interpolation ansatz is of course only a rough approximation, as is the normal force (2.71) itself, but such a simple model is in fact fully sufficient for elastic frictionless wires.

For the implicit solver, one again needs to specify the derivative of (2.72) w.r.t. change of the nodal positions. By the rules of differential calculus, it reads

$$\mathbf{J}_{\text{self},e_1,e_2} = \frac{\partial \mathbf{f}_{\text{self},e_1,e_2}}{\partial \mathbf{p}} = \frac{1}{2}\left(\boldsymbol{\omega} \otimes \mathbf{n}\right)\frac{\partial f_\perp}{\partial \mathbf{p}} + \frac{f_\perp}{2}\left(\frac{\partial \boldsymbol{\omega}}{\partial \mathbf{p}} \otimes \mathbf{n} + \boldsymbol{\omega} \otimes \frac{\partial \mathbf{n}}{\partial \mathbf{p}}\right) \in \mathbb{R}^{12\times 12} \quad (2.74)$$

where

$$\frac{\partial f_\perp}{\partial \mathbf{p}} = -\frac{\partial f_\perp}{\partial D}\frac{\partial |\boldsymbol{\Delta}\mathbf{c}|}{\partial \mathbf{p}} = -2E^*\sqrt{Dr}\,\mathbf{n}^{\mathrm{T}}\frac{\partial \boldsymbol{\Delta}\mathbf{c}}{\partial \mathbf{p}} \in \mathbb{R}^{1\times 12}, \quad (2.75)$$

$$\frac{\partial \mathbf{n}}{\partial \mathbf{p}} = \frac{1}{|\boldsymbol{\Delta}\mathbf{c}|}\left(\mathbb{1}_3 - \mathbf{n}\mathbf{n}^{\mathrm{T}}\right)\frac{\partial \boldsymbol{\Delta}\mathbf{c}}{\partial \mathbf{p}} \in \mathbb{R}^{3\times 12}, \quad (2.76)$$

$$\frac{\partial \boldsymbol{\Delta}\mathbf{c}}{\partial \mathbf{p}} = \left(\boldsymbol{\omega}^{\mathrm{T}} \otimes \mathbb{1}_3\right) + \left(\mathbf{p}_{n_2} - \mathbf{p}_{n_1}\right)\frac{\partial s_1}{\partial \mathbf{p}} - \left(\mathbf{p}_{n_4} - \mathbf{p}_{n_3}\right)\frac{\partial s_2}{\partial \mathbf{p}} \in \mathbb{R}^{3\times 12}. \quad (2.77)$$

This is fairly complex already, which is another reason, aside from sufficiency, why a more elaborate model for $\mathbf{f}_{\text{self}}$ isn't worth the effort. From (2.74–2.77), the Jacobian is fully defined, given that $\frac{\partial s_1}{\partial \mathbf{p}}$ and $\frac{\partial s_2}{\partial \mathbf{p}}$ can be calculated. However, these are exactly the problem. When the two interacting elements are parallel, s_1 and s_2 become ill-defined. In particular, they may jump from one node to the other, rendering $\frac{\partial s_1}{\partial \mathbf{p}}$ and $\frac{\partial s_2}{\partial \mathbf{p}}$ singular and the Newton-Raphson iterations unstable. This is visualized in Figure 2.4. Therefore, the exchange of forces between contacting elements is further simplified in the case of implicit integration in time by distributing the normal force equally to all four nodes, i.e. $\boldsymbol{\omega} = \left[\frac{1}{2}, \frac{1}{2}, -\frac{1}{2}, -\frac{1}{2}\right]^{\mathrm{T}}$, and by discarding

$$\frac{\partial s_1}{\partial \mathbf{p}} = \frac{\partial s_2}{\partial \mathbf{p}} = 0. \quad (2.78)$$
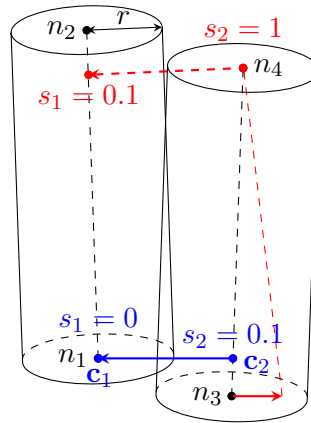

Figure 2.4.: Self-contact of two almost parallel elements, with closest points of approach (blue). A small shift in one of the four nodes may cause the contact parameters s_1, s_2 to jump (red).

3. Program Implementation

3.1. `libMesh` and PETSc

The implementation of the finite element program has been realized with the aid of `libMesh` [36], an open-source C++ library that has gone through active development for more than than eight years. `libMesh` provides basic FEM functionality such as DoF mapping, mesh generation, adaptive mesh refinement and coarsening, matrix and vector assembly, interfaces to various solving techniques, or parallelism (MPI), via a predefined class hierarchy. For this work, I have derived from the `ExplicitSystem` and `NonlinearImplicitSystem` classes to implement the dedicated model described in Chapter 2. `libMesh` supports the Portable, Extensible Toolkit for Scientific Computation (PETSc) [37], which has also been exploited.

The efforts in the present work gave rise to a number of bugfixes and feature enhancements in the official `libMesh` development, notably trunk revisions 4199, 4200, 4210, 4223, 4224, 4238, 4239, 4273, and 4280.

In the following sections, the most essential algorithms and parts of the program that have not been covered in Chapter 2 are detailed. The main focus is on the two implemented schemes for the integration in time (Section 3.2), as well the search for potentially touching wire element pairs (Section 3.4).

3.2. Time Integration

Newmark's family of integration schemes [11] is widely used for solving hyperbolic equilibrium equations in structural dynamics [38, 39]. Depending on the choice of its two parameters, $\beta, \gamma \in [0, 1]$, it can be made implicit or explicit, and absolutely stable or conditionally stable. In the Newmark method, the solution vector and its time derivatives are discretized and integrated according to

$$\mathbf{u}(t + \Delta t) \approx \mathbf{u}_{t+\Delta t} = \mathbf{u}_t + \Delta t\, \dot{\mathbf{u}}_t + \frac{(\Delta t)^2}{2}\big((1 - 2\beta)\ddot{\mathbf{u}}_t + 2\beta\ddot{\mathbf{u}}_{t+\Delta t}\big), \qquad (3.1)$$

$$\dot{\mathbf{u}}(t + \Delta t) \approx \dot{\mathbf{u}}_{t+\Delta t} = \dot{\mathbf{u}}_t + \Delta t\big((1 - \gamma)\ddot{\mathbf{u}}_t + \gamma\ddot{\mathbf{u}}_{t+\Delta t}\big), \qquad (3.2)$$

As usually, Δt denotes the finite time step, and the accelerations at time t are given by

$$\ddot{\mathbf{u}}(t) \approx \ddot{\mathbf{u}}_t = \mathbf{M}^{-1}\big(\mathbf{f}_{\text{ext}}(\mathbf{u}_t) - \mathbf{C}\dot{\mathbf{u}}_t - \mathbf{K}(\mathbf{u}_t)\mathbf{u}_t\big). \qquad (3.3)$$

Implicit Integration

For the implicit integration, the unconditionally stable *constant-average acceleration method* that is obtained by setting $\beta = 0.25$ and $\gamma = 0.5$ is chosen. In this case, the system of ordinary differential equations (2.1) reduces to the system of algebraic equations [39]

$$\bar{\mathbf{K}}_{t+\Delta t}\mathbf{u}_{t+\Delta t} = \bar{\mathbf{f}}_{t,t+\Delta t} \tag{3.4}$$

with

$$\bar{\mathbf{K}}_{t+\Delta t} = \mathbf{K}(\mathbf{u}_{t+\Delta t}) + a_0\,\mathbf{M} + a_1\,\mathbf{C}, \tag{3.5}$$

$$\bar{\mathbf{f}}_{t,t+\Delta t} = \mathbf{f}_{\text{ext}}(\mathbf{u}_{t+\Delta t}) + \mathbf{M}\,\mathbf{a}_t + \mathbf{C}\,\mathbf{b}_t, \tag{3.6}$$

$$\mathbf{a}_t = a_0\,\mathbf{u}_t + a_2\,\dot{\mathbf{u}}_t + a_3\,\ddot{\mathbf{u}}_t, \tag{3.7}$$

$$\mathbf{b}_t = a_1\,\mathbf{u}_t + a_4\,\dot{\mathbf{u}}_t + a_5\,\ddot{\mathbf{u}}_t, \tag{3.8}$$

and Newmark coefficients

$$a_0 = \frac{1}{\beta\,(\Delta t)^2}, \quad a_1 = \frac{\gamma}{\beta\Delta t}, \quad a_2 = \frac{1}{\beta\Delta t}, \tag{3.9}$$

$$a_3 = \frac{1}{2\beta} - 1, \quad a_4 = \frac{\gamma}{\beta} - 1, \quad a_5 = \Delta t\left(\frac{\gamma}{2\beta} - 1\right). \tag{3.10}$$

In each implicit timestep, the nonlinear system of equations (3.4) needs to be solved. To this end, the line search solver provided by PETSc is used in combination with the Newton-Raphson method for the direction of descent. Ultimately, `libMesh`'s interface to the solver requires two callback functions to be specified. The first function computes the residual vector based on the current iterated guess for $\mathbf{u}_{t+\Delta t}$,

$$\mathbf{r}_{t,t+\Delta t} = \bar{\mathbf{K}}_{t+\Delta t}\mathbf{u}_{t+\Delta t} - \bar{\mathbf{f}}_{t,t+\Delta t}, \tag{3.11}$$

where the external forces in $\bar{\mathbf{f}}_{t,t+\Delta t}$ are assembled according to

$$\mathbf{f}_{\text{ext}} = \bigoplus_n \mathbf{f}_{\text{cav},n} + \bigoplus_{(e_1,e_2)} \mathbf{f}_{\text{self},e_1,e_2}. \tag{3.12}$$

$\mathbf{f}_{\text{cav},n}$ are the nodal forces due to cavity contacts from (2.53), and $\mathbf{f}_{\text{self},e_1,e_2}$ are the forces due to self-contacts from (2.72). $\bigoplus$ denotes the subvector/submatrix assembly operation mentioned in the beginning of Chapter 2. The second callback function provides the Jacobian

$$\mathbf{J}_{t,t+\Delta t} = \frac{\partial \mathbf{r}_{t,t+\Delta t}}{\partial \mathbf{u}_{t+\Delta t}} = a_0\,\mathbf{M} + a_1\,\mathbf{C} + \bigoplus_e \mathbf{K}_{\text{t},e} - \bigoplus_n \mathbf{J}_{\text{cav},n} - \bigoplus_{(e_1,e_2)} \mathbf{J}_{\text{self},e_1,e_2}, \tag{3.13}$$

where $\mathbf{K}_{\text{t},e}$ are the corotational element tangent stiffness matrices from (2.41), $\mathbf{J}_{\text{cav},n}$ are the nodal Jacobians due to cavity contacts from (2.64), and $\mathbf{J}_{\text{self},e_1,e_2}$ are the Jacobians due to self-contacts from (2.74) for all contact pairs (e_1, e_2). Upon convergence to the

new solution $\mathbf{u}_{t+\Delta t}$, the corresponding velocity and acceleration vectors are calculated using

$$\ddot{\mathbf{u}}_{t+\Delta t} = a_0(\mathbf{u}_{t+\Delta t} - \mathbf{u}_t) - a_2\,\dot{\mathbf{u}}_t - a_3\,\ddot{\mathbf{u}}_t, \tag{3.14}$$

$$\dot{\mathbf{u}}_{t+\Delta t} = \dot{\mathbf{u}}_t + a_6\,\ddot{\mathbf{u}}_t + a_7\,\ddot{\mathbf{u}}_{t+\Delta t}, \tag{3.15}$$

where

$$a_6 = (1 - \gamma)\,\Delta t, \quad a_7 = \gamma\Delta t. \tag{3.16}$$

Explicit Integration

For the explicit scheme, the constant-average acceleration method is implement in combination with an adaptive timestepping predictor-corrector algorithm based on an *a posteriori* local error estimator by Zienkiewicz and Xie [38, 40]. The prediction step is obtained from the explicit part of (3.1) and (3.2):

$$\mathbf{u}_{t+\Delta t}^{\mathrm{p}} = \mathbf{u}_t + \Delta t\,\dot{\mathbf{u}}_t + \frac{(\Delta t)^2}{2}(1 - 2\beta)\ddot{\mathbf{u}}_t, \tag{3.17}$$

$$\dot{\mathbf{u}}_{t+\Delta t}^{\mathrm{p}} = \dot{\mathbf{u}}_t + \Delta t(1 - \gamma)\ddot{\mathbf{u}}_t, \tag{3.18}$$

$$\ddot{\mathbf{u}}_{t+\Delta t}^{\mathrm{p}} = \mathbf{M}^{-1}\big(\mathbf{f}_{\mathrm{ext}}(\mathbf{u}_{t+\Delta t}^{\mathrm{p}}) - \mathbf{C}\dot{\mathbf{u}}_{t+\Delta t}^{\mathrm{p}} - \mathbf{K}(\mathbf{u}_{t+\Delta t}^{\mathrm{p}})\mathbf{u}_{t+\Delta t}^{\mathrm{p}}\big). \tag{3.19}$$

Based on the predicted acceleration, the predicted solution and velocity are corrected by the previously omitted part:

$$\mathbf{u}_{t+\Delta t}^{\mathrm{c}} = \mathbf{u}_{t+\Delta t}^{\mathrm{p}} + \mathbf{u}_t + (\Delta t)^2\beta\,\ddot{\mathbf{u}}_{t+\Delta t}^{\mathrm{p}}, \tag{3.20}$$

$$\dot{\mathbf{u}}_{t+\Delta t}^{\mathrm{c}} = \dot{\mathbf{u}}_{t+\Delta t}^{\mathrm{p}} + \Delta t\,\gamma\,\ddot{\mathbf{u}}_{t+\Delta t}^{\mathrm{p}}. \tag{3.21}$$

A simple estimator for the relative local error made by performing such a step is then given by

$$\eta_{t+\Delta t} = \left(\beta - \frac{1}{6}\right)(\Delta t)^2\frac{\|\ddot{\mathbf{u}}_{t+\Delta t}^{\mathrm{p}} - \ddot{\mathbf{u}}_t\|_{L^\infty}}{\|\mathbf{u}_{t+\Delta t}^{\mathrm{c}} - \mathbf{u}_t\|_{L^\infty}}, \qquad \beta \neq \frac{1}{6}, \tag{3.22}$$

where $\|\cdot\|_{L^\infty}$ denotes the Chebyshev distance. Ideally, the tradeoff between large timestep and large error is dealt with in such a way that the local error is approximately constant over time. Zienkiewicz and Xie found that this can be efficiently achieved by applying the following adaptive timestepping rules, given a desired target value η for the relative local error, a maximum tolerated one $\eta_{\max} > \eta$, and a lower bound $\eta_{\min} < \eta$ above which the timestep is considered large enough:

- If $\eta_{t+\Delta t} > \eta_{\max}$, reject the timestep and repeat with $\Delta t := \left(\frac{\eta}{\eta_{t+\Delta t}}\right)^{\frac{1}{3}}\Delta t$.

- If $\eta_{t+\Delta t} < \eta_{\min}$, accept the step by setting $\mathbf{u}_{t+\Delta t} = \mathbf{u}_{t+\Delta t}^{\mathrm{c}}$, $\dot{\mathbf{u}}_{t+\Delta t} = \dot{\mathbf{u}}_{t+\Delta t}^{\mathrm{c}}$, $\ddot{\mathbf{u}}_{t+\Delta t} = \ddot{\mathbf{u}}_{t+\Delta t}^{\mathrm{p}}$, but continue with a larger timestep $\Delta t := \left(\frac{\eta}{\eta_{t+\Delta t}}\right)^{\frac{1}{3}}\Delta t$.

- Otherwise, accept without modifying Δt.

$\eta_{\min} = 10^{-5}$, $\eta = 10^{-4}$ and $\eta_{\max} = 10^{-3}$ yields reasonable performance.

Boundary and Initial Conditions

Boundary conditions are imposed by penalizing any bending deflection v_n, w_n on nodes that are still outside the cavity. The penalty term that adds to the stiffness matrix to this end is taken to be that of regular cavity contacts,

$$k_{\text{cav}} = \frac{\pi}{4} E^* \bar{h}, \tag{3.23}$$

see (2.53). This models a thin cylindrical pipe through which the wire is injected into the cavity. In addition, the outermost node $n = N$ is clamped by applying another penalty stiffness

$$k_{\text{clamp}} = \frac{EI}{h_N} \tag{3.24}$$

to θ_N and ψ_N. The morphological order of the constrained wire is governed by its internal twist [10], which can be controlled by introducing an optional penalty stiffness on φ_N,

$$k_{\text{twist}} = \frac{GJ}{h_N}. \tag{3.25}$$

To push the wire into the cavity at constant velocity v_{push}, I set $\dot{u}_N(t) \equiv v_{\text{push}}$ and $\ddot{u}_N(t) \equiv 0$.

The simulations are started with an undeformed straight wire in equilibrium along the global x-axis, i.e. $\mathbf{u}(0) \equiv \dot{\mathbf{u}}(0) \equiv \ddot{\mathbf{u}}(0) \equiv \mathbf{0}$ except that $\dot{u}_n(0) = v_{\text{push}}$ for all nodes n, and that the initial axial symmetry is broken by giving at least two nodes a small random perturbation perpendicular to the axis. The nodal quaternions are initialized to $\mathbf{q}_n = [1, 0, 0, 0]^{\text{T}}$ for all nodes n.

3.3. Dynamic Mesh Enlargement

In order to save a significant amount of computation time while the packing density is still small, the simulation starts off with a small mesh, i.e. low N, and dynamically extends it by appending new elements when necessary. To the present day, modifications of the mesh domain are not officially supported by `libMesh`. However, only small extensions to the source code were necessary to enable this feature, that is vital in the case of increasingly packed cavities.

Whenever the number of wire elements that hasn't entered the cavity yet drops below a certain minimum number, the mesh is enlarged by a few nodes and elements at its outer end. All vector quantities such as the solution, velocities etc. then need to be copied to larger containers. The new degrees of freedom are oriented in perfect x-direction, and their axial displacements u_n are initialized such that the current average longitudinal compression of the wire outside the cavity is preserved. In case of free twist $k_{\text{twist}} = 0$, the same procedure applies to φ_n, i.e. the quaternions $\mathbf{q}_n$, preserving the average internal twist of the wire outside the cavity.

The program is also capable of pulling the wire out of the cavity again. A few elements can be cut off from the outer end of the mesh as soon as the number of wire elements outside the cavity exceeds a certain maximum value, increasing the performance of the simulation. By construction in `libMesh`, this also requires the remaining parts of all vectors to be copied to new data structures. It will be found in Chapter 4 that this overhead is very small compared to the overall speedup, and that the whole mesh modification effort pays off very well.

3.4. Efficient Self-Contact Search

In this section, an important part of the simulation program, the search for touching element pairs (e_1, e_2), is addressed. Since the number of contacts grows like the square of the packing density in the uncorrelated thin rod limit in 3D [41], an efficient treatment of these pairs is crucial for performance. Serial processing is in the focus rather than parallelization, for reasons discussed in the next section.

Distance between Two Elements

In Section 2.7 the indentation depth $D = 2r - |\mathbf{c}_1 - \mathbf{c}_2|$ was used for the calculation of self-contact forces, where

$$
\begin{aligned}
\mathbf{c}_1 &= \mathbf{p}_{n_1} + s_1(\mathbf{p}_{n_2} - \mathbf{p}_{n_1}), \quad s_1 \in [0, 1], \\
\mathbf{c}_2 &= \mathbf{p}_{n_3} + s_2(\mathbf{p}_{n_4} - \mathbf{p}_{n_3}), \quad s_2 \in [0, 1]
\end{aligned}
\tag{3.26}
$$

are the closest points of approach on the center lines of two linearized wire elements. Finding the distance between two line segments, or finding the segment parameters s_1 and s_2, is a nontrivial task. I have implemented a modified version of the quadric algorithm by Sunday [42], which provides an efficient implementation based on a note by Eberly [43]. The modification consists of normalizing the two line segments to unit length, which fixes the faulty detection of parallel lines for short segments in Sunday's algorithm.

Finding the Contacting Element Pairs

From a naive perspective, the problem of finding all pairs of close particles is an $\mathcal{O}(N^2)$ task. The use of *linked cell lists* [44] reduces this complexity to $\mathcal{O}(N)$, which has made them an integral part of modern molecular dynamics. For the problem of finding touching wire elements, a slightly extended version of the original linked cell method is applied. The algorithm decomposes the bounding box of the ellipsoidal cavity into cubic cells of equal edge length α (Figure 3.1). Each mesh element is then assigned to the cell in which the effective position of its left node, $\mathbf{p}_1$, lies. By choosing the cell size

$$
\alpha \geq 2(r + \max_e h_e),
\tag{3.27}
$$

it is assured that all elements e_2 potentially penetrating an element e_1 can be found in either the cell of e_1 or one of its $26 = 3^3 - 1$ neighboring cells. If α is set such that (3.27) holds *equally*, the linked cell lists need to be rebuilt or at least updated in each timestep, which is quite costly. With implicit integration in time, it's even much worse, as the cells would have to be rebuilt or updated every time the residual is evaluated during the line search, in each iteration of the Newton-Raphson method, for each timestep. Therefore, each cell is granted a margin $\delta > 0$:

$$
\alpha = 2(r + \max_e h_e) + \delta.
\tag{3.28}
$$

This way, the cell affiliation is valid as long as the cumulated maximum nodal displacement doesn't exceed $\frac{\delta}{2}$. The best choice for δ strongly depends on the length scales and the amount of translational kinematics, and it can even vary with the packing density. Setting $\delta \approx r$ proved to be a reasonable rule of thumb.

After the linked cell lists have been constructed, the number of potentially interacting element pairs can be reduced further by rejecting those who are too far apart despite belonging to neighboring cells. Consistently with (3.28), all pairs (e_1, e_2) for which $|\Delta\mathbf{c}| > 2r + \delta$ holds are thrown away. Furthermore, pairs that are close to each other in the chain of wire elements need to be excluded, which is important in the case of short element lengths $h \leq 2r$ or large longitudinal compression.
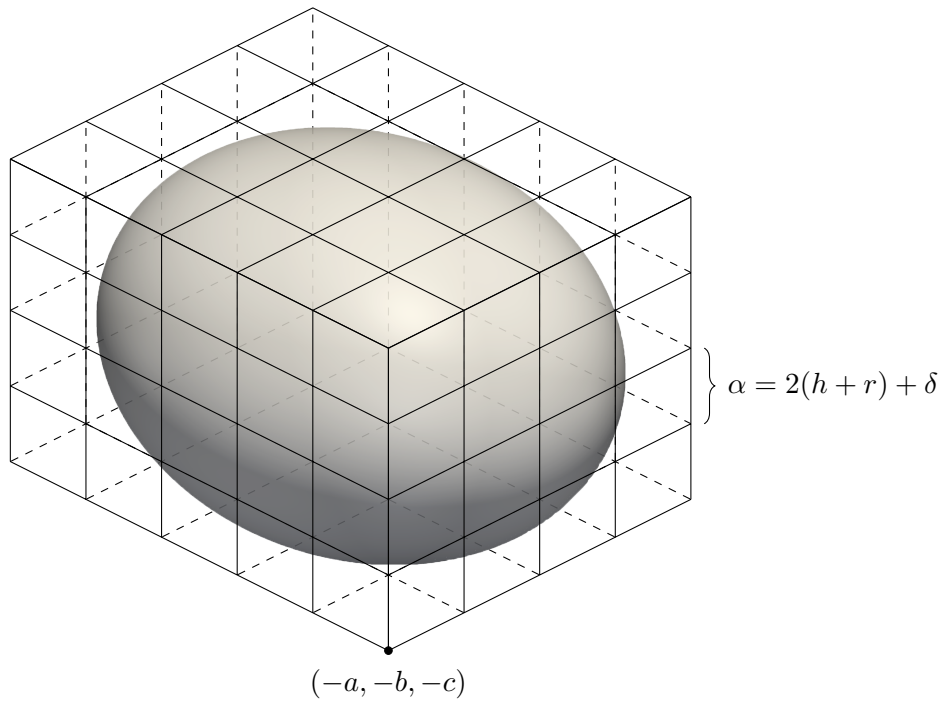

Figure 3.1.: Visualization of the linked cell method: Spatial decomposition of the cavity into a regularly spaced cubic grid.

3.5. Parallelization

`libMesh` and PETSc support parallel processing using the Message Passing Interface (MPI) standard. A one-dimensional mesh like the one used for rods in this work is particularly suited for parallelization, because mesh partitioning is trivial and the subdomain interfaces causing interprocess communication are usually limited to only $\mathcal{O}(p)$ nodes, where p is the number of processors, independent of the mesh size or wire length. Thus, at first glance, one could be tempted to expect a very high parallel efficiency for the finite element program. Unfortunately, this is not at all the case, for the following reason. *A priori*, self-contact may arise between almost any two elements at any time. While the linked cell lists provide a naturally parallelizable spatial decomposition of self-contacts, the *construction* of the cells requires knowledge about the positions $\mathbf{p}_n$ of *all* nodes. Either before or after filling the cells, they *all* need to be communicated among the processors. This is a mere consequence of two completely diverse spatial arrangements intrinsic to the problem of long densely packed rods: On the one hand, each element propagates its stiffness to the neighboring elements and thus the mesh is inherently linearly partitioned into p blocks of N/p consecutive elements, but on the other hand, self-contacts happen in real space, which is completely decoupled from the wire contour. Even if the potentially touching element pairs are sought only once every few thousand timesteps thanks to the cell margin δ, the current nodal positions must be communicated in *each* timestep to determine the indentation depth and force direction. Since there are up to $\mathcal{O}(N^2)$ contacts in a densely packed cavity, parallel efficiency is effectively destroyed.

With this said, it is nevertheless possible to solve (2.1) in parallel, albeit very inefficiently. Indeed, the program presented in this thesis has been implemented with support for parallelism and small test systems have been successfully simulated in parallel. The construction of the linked cells simply happens in serial mode after all nodal positions have been communicated among the processors. Each processor then calculates the contact forces for all elements involved in self-contacts, which fall into its realm, based on the repeatedly communicated nodal positions.

3.6. Flowcharts

The following flowcharts show the major steps within the simulation program to provide a better understanding of the program structure and computational workflow depending on the choice for the integration scheme. For clarity, minor conditionals or subroutines, optimization details like object caching, and technicalities related to `libMesh` or parallelism are omitted. Figure 3.2 visualizes the outermost program loop that is responsible for generic timestepping. In Figure 3.3, the explicit adaptive predictor-corrector timestep is outlined. The implicit analogon is shown in Figure 3.4, where a deeper nesting of loops for the nonlinear Newton-Raphson scheme becomes evident.
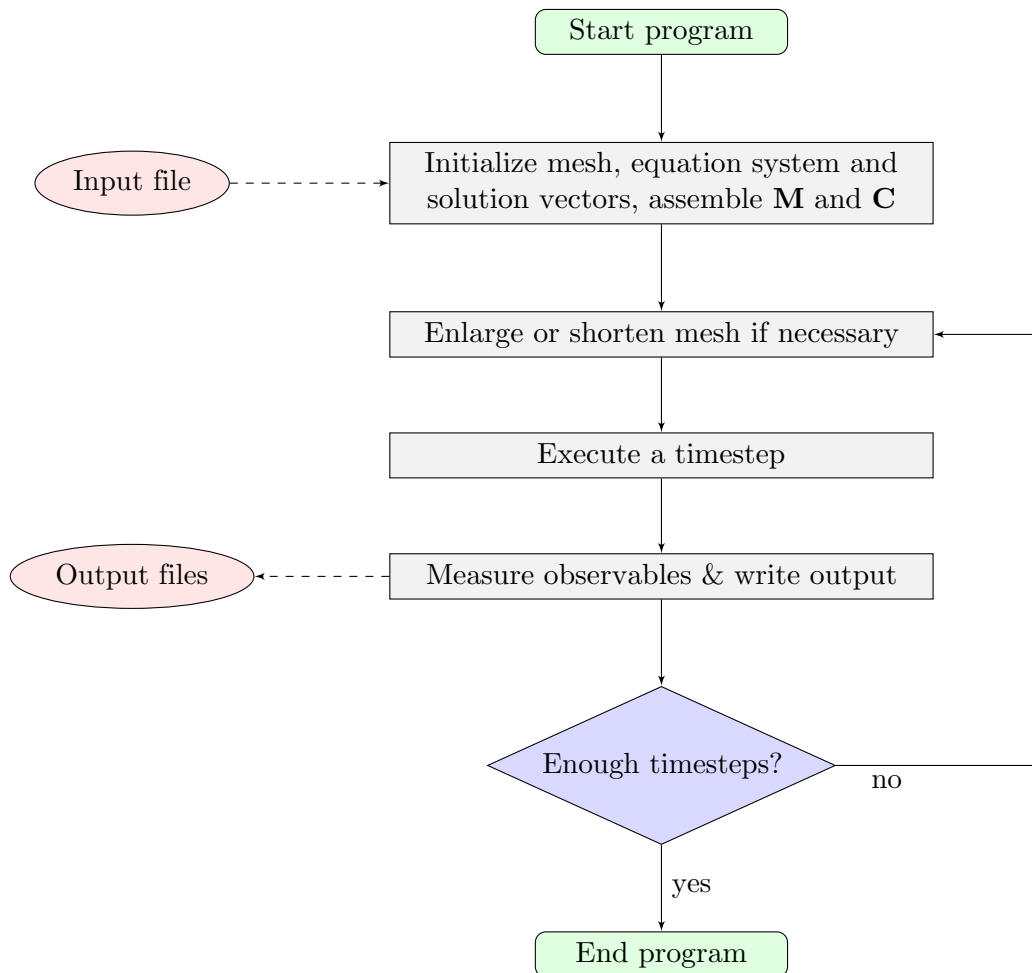
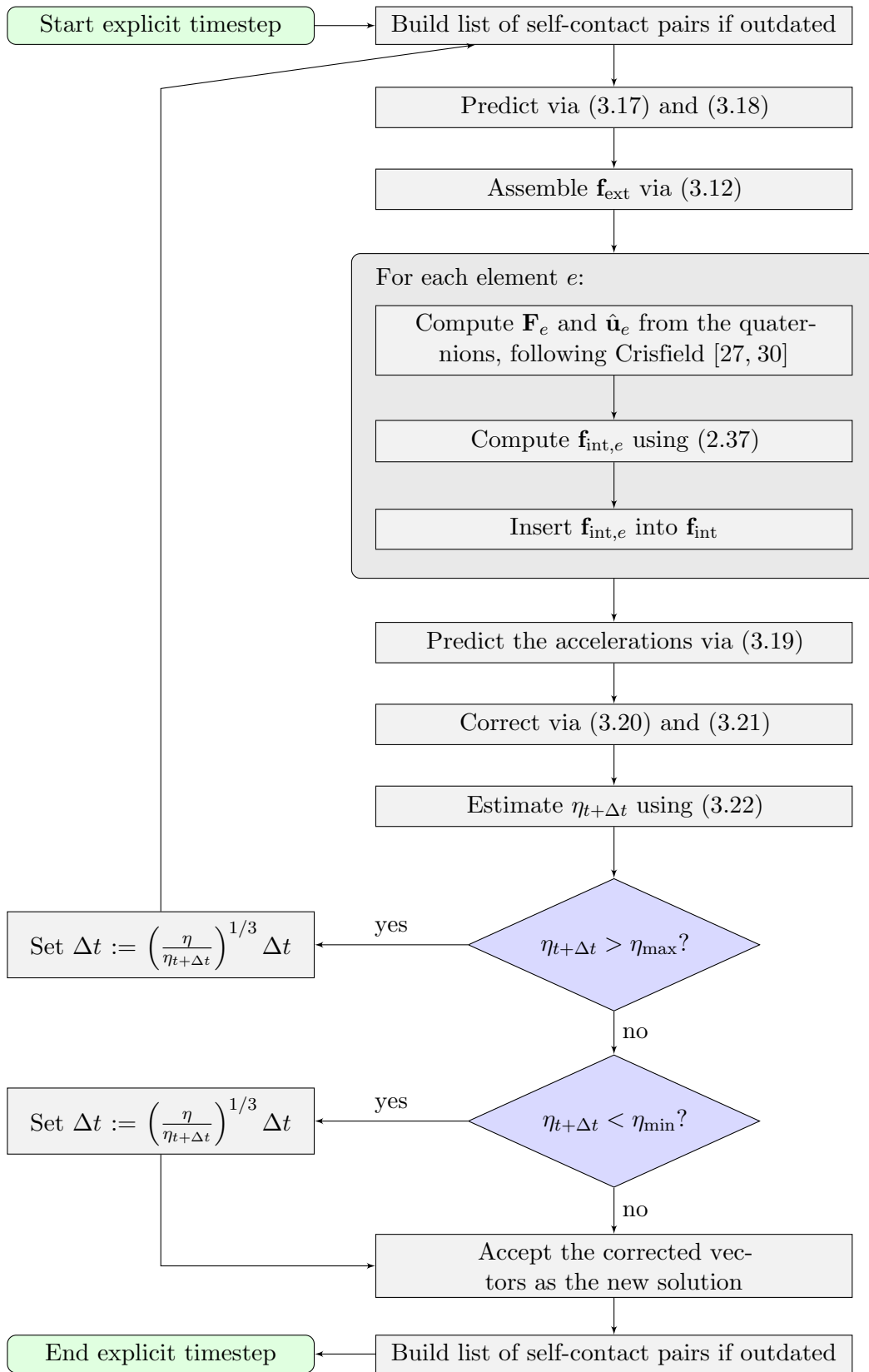**Figure 3.2.:** Flowchart of the overall program structure.

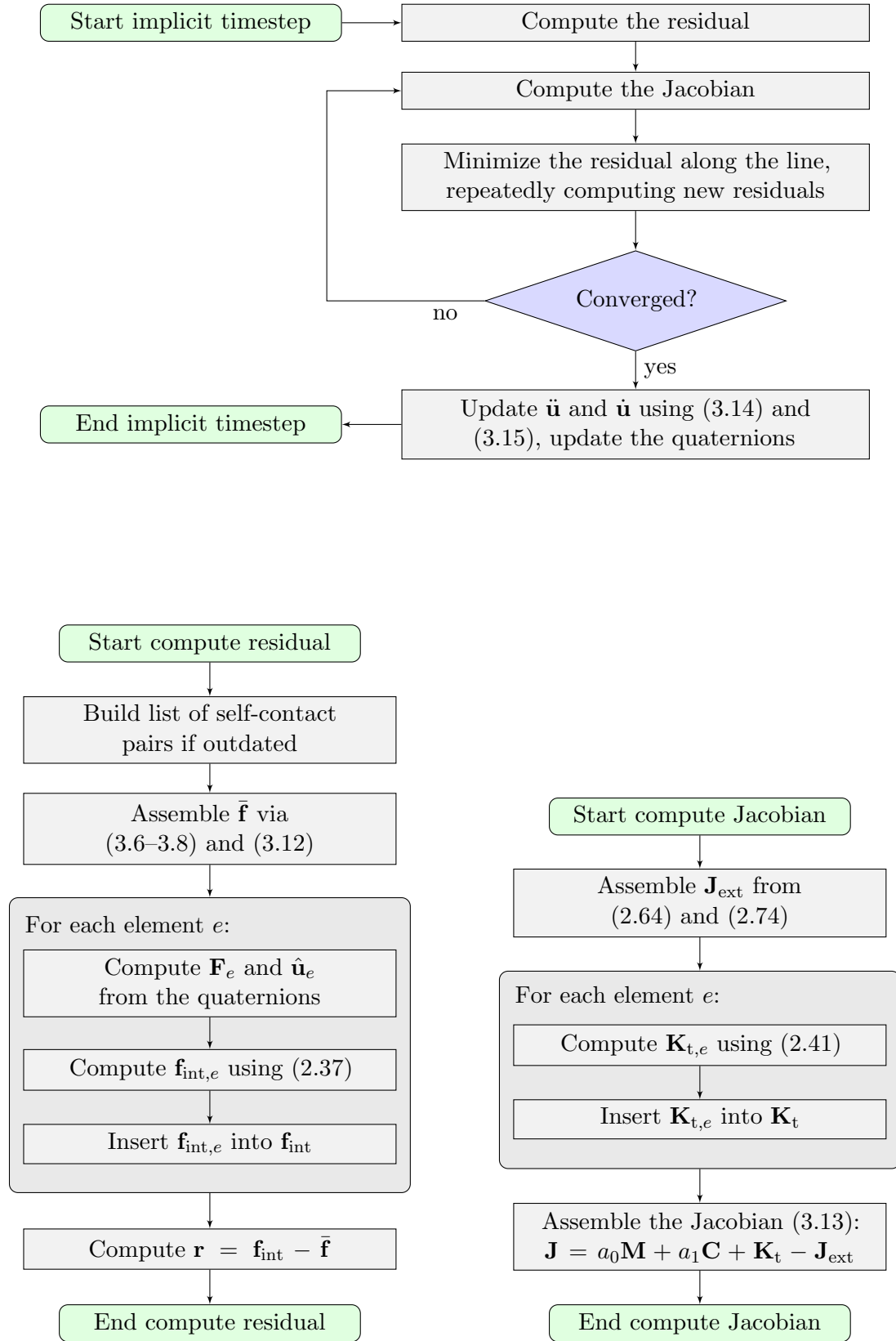**Figure 3.3.:** Flowchart of a timestep in the explicit predictor-corrector scheme.

Figure 3.4.: Flowchart of a timestep in the implicit scheme with callback subroutines.

4. Benchmarks & Results

4.1. Verification of the Corotated Beams

Before meaningful physics can be done, the implementations need to be verified. In particular the lengthy technical corotation components are somewhat prone to small errors with large impacts. I have successfully reproduced examples 1 and 2 in Crisfield's paper [27], which have served as static test cases for various implementations of corotated beams, Refs. [25, 45–47] being only the first ones in a long series. Example 1, *cantilever subject to an end moment*, is not shown here.

Test Case A

In example 2, a *45 degree bend*, a thin Euler-Bernoulli beam with intrinsic curvature $\kappa = 1/R$, $R = 100$, forming a 45 degree bend, is clamped at the origin ($\mathbf{u}_0(t) \equiv \mathbf{0}$). An increasing external tip load Q is applied perpendicular to the curvature, resulting in a three-dimensional bending response. The relevant material and geometry parameters are $E = 10^7$, $I = 1$, $\nu = 0$, $N = 8$. Figure 4.1 shows the resulting static equilibrium solutions for $Q = 300, 450, 600$, which are consistent with Crisfield's results within convergence tolerance. Note that the intrinsic curvature leading to

$$\mathbf{u}_n(0) = [R(1 - \sin\theta_n), 0, R(1 - \cos\theta_n), 0, \theta_n, 0]^{\mathrm{T}}, \qquad \theta_n = \frac{\pi}{4}\frac{n}{N}, \qquad (4.1)$$

can easily be established within the corotational framework by subtracting the initial local rotations

$$\hat{\theta}_1^0 = -\frac{\pi}{8}, \qquad \hat{\theta}_2^0 = \frac{\pi}{8} \qquad (4.2)$$

in (2.34) for each element.

Test Case B

To verify the corotational formula (2.46) for the bending energy, a simple circular setup similar to Crisfield's first example is used, where the exact solution is available. A cantilever EBT beam with $N = 20$ elements, clamped at the origin, is subjected to end moments $M_k = \frac{k}{6}\frac{EI}{R}$, $k = 0, 1, ..., 6$, resulting in the bending energy

$$U_{\mathrm{b},k} = \frac{1}{2}\int_0^L \frac{M_k^2}{EI}\,\mathrm{d}s = \left(\frac{k}{6}\right)^2 \pi\frac{EI}{R}, \qquad (4.3)$$

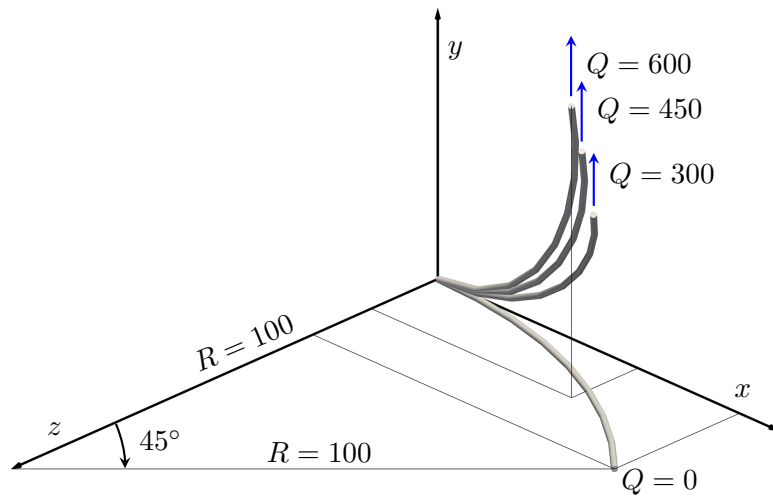which is nicely numerically recovered. The configuration is visualized in Figure 4.2.

Figure 4.1.: 45 degree corotated Euler-Bernoulli bend subject to concentrated transverse tip load
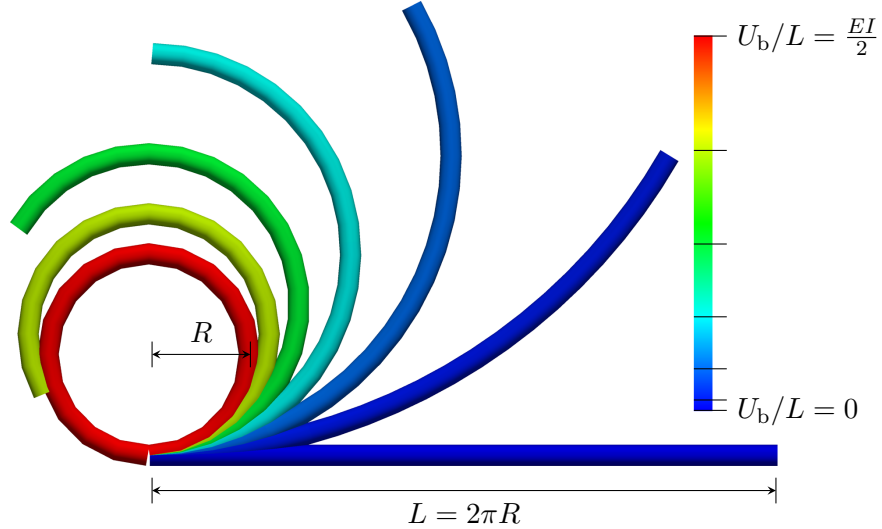

Figure 4.2.: Bending energy density of a cantilever beam with 20 elements and final curvature $\kappa = 1/R$ subject to an inreasing end moment.

Test Case C

As a final three-dimensional stress test of the corotational coupling of twist, axial displacement and bending deflections, which are independent in linear beam theory, it is demonstrated here how an increasing external torque is capable of writhing a wire. An initially straight cylindrical third-order beam (RBT) with tiny random deflection to break axial symmetry is clamped at the origin ($\mathbf{u}_0(t) \equiv \mathbf{0}$). The other end is constrained to the x-axis according to

$$\mathbf{u}_{20}(t) = [u(t), 0, 0, \varphi(t), 0, 0]^{\mathrm{T}}. \tag{4.4}$$

The simulation parameters are $E = 10^7$, $I = 1$, $r = (4/\pi)^{1/4}$, $\nu = 0$, $N = 20$, $\rho = 10^{-3}$. The wire is integrated implicitly in time with $\Delta t = 10^{-3}$ and viscous damping factor $c_\mathrm{v} = 0.3$; self-contacts are switched off. The angle of twist $\varphi(t)$ at the end node is increased with time until it is large enough to cause the two ends to pass through each other, resulting in a ring-shaped static equilibrium state. This critical value has been determined to be $1.375 < \varphi_\mathrm{crit}/2\pi < 1.376$ for the above settings, and therefore

$$\varphi(t) = 2\pi \min\{t, 1.376\}. \tag{4.5}$$

The resulting time evolution is illustrated in Figure 4.3.

(a) $t = 1.5$ (b) $t = 2.1$ (c) $t = 2.23$

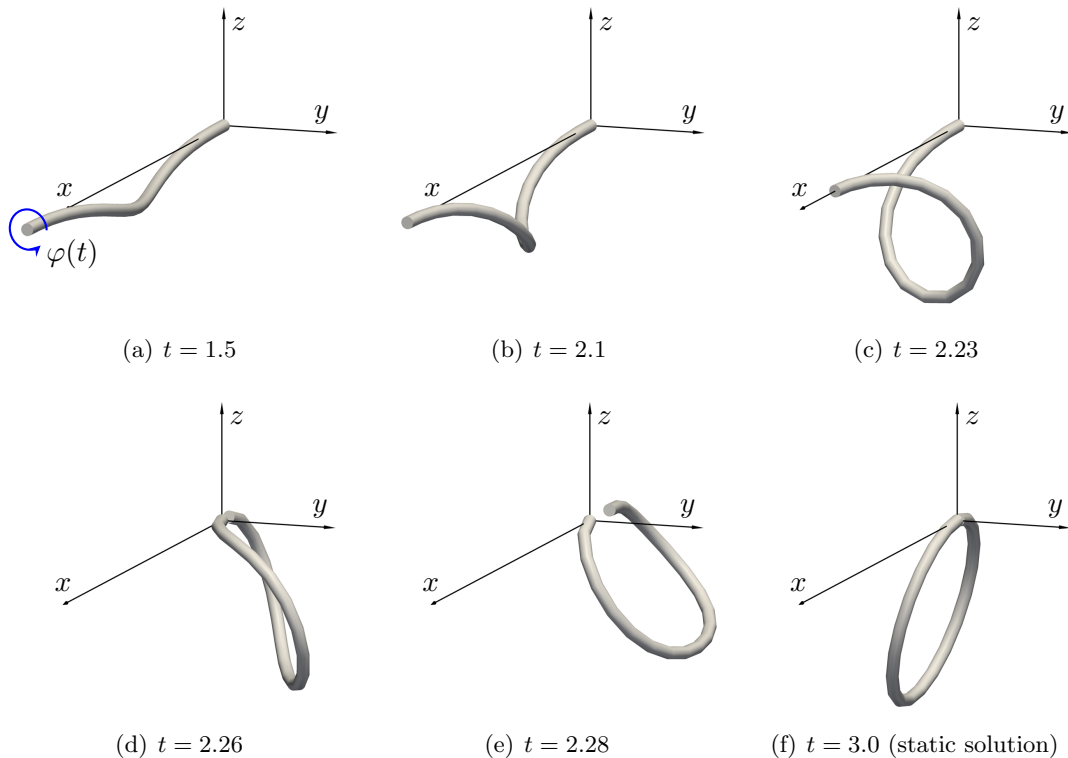(d) $t = 2.26$ (e) $t = 2.28$ (f) $t = 3.0$ (static solution)

Figure 4.3.: Qualitative stress test of the corotational formulation: Three-dimensional response of a circular third-order beam to an increasing twist. All shown states except the last are out of equilibrium.

4.2. h-**Convergence**

This section is briefly concerned with the convergence of the corotated finite element beams to the continuum solution with decreasing mesh spacing $h \to 0$, as yet another way of verifying correctness of the program. The two-dimensional bending of a cantilever beam clamped at the origin is simulated, with $E = 10^7$, $I = 1$, $L = 100$, using both EBT and RBT subject to different load cases. The exact solution for two-dimensional linear Euler-Bernoulli beams can be found for numerous boundary conditions and applied external loads in many text books, such as Ref. [48]. For a beam of length L with a single clamped end, subject to a concentrated tip load Q, it is given by

$$w(Q; x) = \frac{Q}{EI} \frac{x^2(3L - x)}{6}, \tag{4.6}$$

while for a uniform load distribution $q(x) \equiv q$ it reads

$$w(q; x) = \frac{q}{EI} \frac{x^2(6L^2 - 4Lx + x^2)}{24}. \tag{4.7}$$

For simplicity, the corotated cylindrical beams are verified such that linear EBT predicts a maximal deflection of $w(x{=}L) = 5, 10, 15$, i.e. $Q = 150, 300, 450$ and $q = 4, 8, 12$. The results for these loads are plotted in Figure 4.4 for $N = 3$ and $N = 5$ elements. For thin beams, the difference between the beam theories is very small, which is why the curves for CR-EBT and CR-RBT almost coincide, in particular in the case of uniformly distributed load.

For measuring the convergence of the finite element solution to the continuum solution, the unknown maximum static deflection of the tip of a nonlinear continuum beam is approximated by the solution obtained with 100 elements. The relative error as a function of the number of elements is then given by

$$\varepsilon(N) = \left| \frac{w_N}{w_{100}} - 1 \right| \propto N^{-p}, \tag{4.8}$$

and an algebraic convergence rate $p = 2$ is expected. Note that since node 0 is clamped, the number of degrees of freedom is $6N$, i.e. directly proportional to the number of elements. The expected quadratic behavior can be observed in all cases very nicely, with fitted rates ranging from $p = 2.01$ to $p = 2.06$, as shown in Figure 4.5.
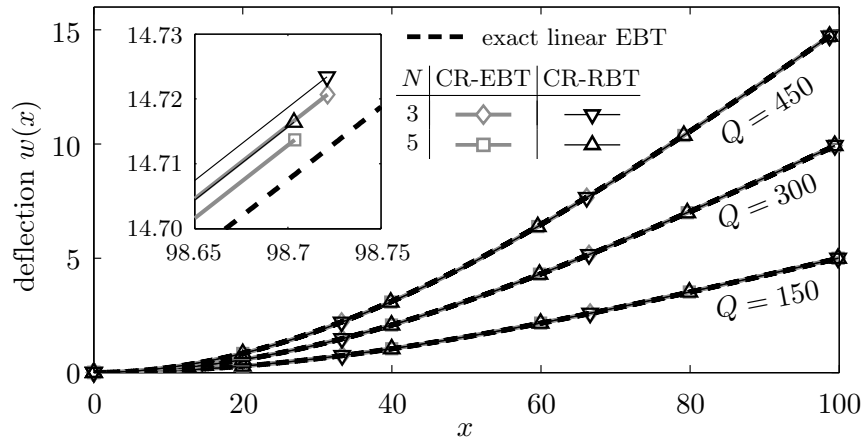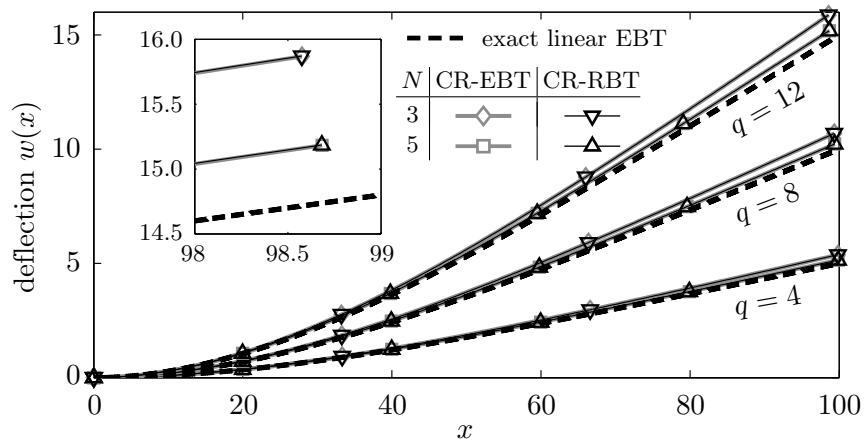
(a) Concentrated end load Q

(b) Uniform load distribution q

Figure 4.4.: Comparison of corotated beam theories in 2D for different load cases. Note the aspect ratio of the two axes. The markers denote the nodes, while the connecting solid lines correspond to the corotated cubic Hermite interpolation of the beam center lines. In the insets the beam tip of the respective highest load case is magnified for better visibility of the differences.
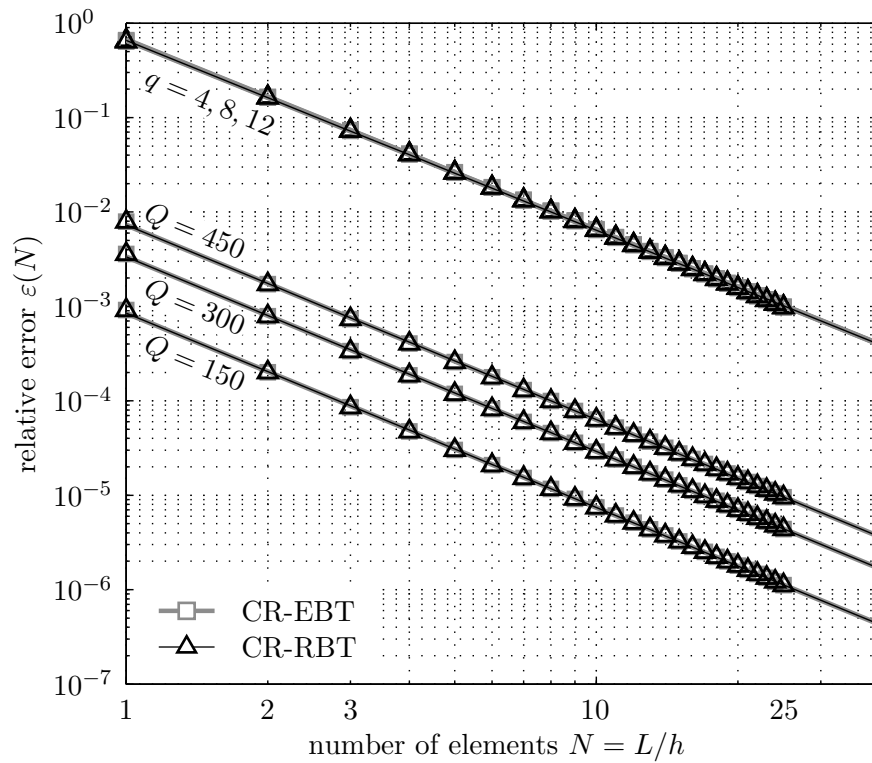
Figure 4.5.: Quadratic convergence in h of the finite element wire for the six load cases from Figure 4.4 for corotated Euler-Bernoulli and third order beam theory. The relative error ε of the static end point deflection is plotted against the number of elements $N = \{1, 2, ..., 25\}$, on a double-logarithmic scale. The data for the uniform load distribution lie on top of each other, as do CR-EBT and CR-RBT in all cases for such thin beams.

4.3. Explicit vs. Implicit Integration

An essential part of this thesis is the comparison between implicit and explicit integration in time. The two schemes described in Section 3.2 reveal fundamentally different suitability for the problem of dense packing of wires in two- or three-dimensional cavities. These findings are summarized in this section.

The first focus is on a severe fundamental problem of the technical kind appearing in wire-wire contacts in implicit integration. Probably like any other comparable FEM software, `libMesh` and PETSc fix the sparsity pattern of the Jacobian (3.13) and all other matrices based on the mesh topology and element interconnectivity at the beginning of the simulation. For the wire mesh at hand, no memory is allocated for the off-diagonal blocks connecting two elements unless they are neighbors. *A priori*, self-contact may arise between almost any two elements at any time, though. Thus, in order to insert the full 12×12 Jacobian (2.74) arising from two interacting elements into the global $6(N+1) \times 6(N+1)$ system Jacobian, the latter either needs to be dense, which makes the Newton-Raphson iterations beyond expensive, or the sparsity pattern needs to dynamically adapt to the evolving pairs of interacting elements. Apart from not being currently supported in `libMesh`, changes in the sparsity pattern in *each* Newton-Raphson iteration, for *each* timestep, are presumably too expensive to be a valid option, especially when the number of self-contacts approaches $\mathcal{O}(N^2)$ for dense packings. In other words, one is left with the fact that only half of the self-contact Jacobian, namely the two 6×6 blocks on the diagonal, can be used in the overall Jacobian. The off-diagonal blocks dictating the change of contact forces acting on one element w.r.t. change of position of the other, are lost, with fatal consequences for the convergence behavior.

Let's consider an example to visualize what this implies in practice. A two-dimensional spherical cavity with effective size $r_{\mathrm{cav}}/r = 50$ is packed. With the explicit predictor-corrector scheme with adaptive timestepping such that $\Delta t \approx 0.057$ on average at a maximum local step error tolerance $\eta_{\max} = 10^{-3}$, the dense packing regime is accessible without complications, as visible in Figure 4.6(a). The implicit integrator with significantly smaller timestep $\Delta t = 10^{-3}$, however, soon suffers from convergence problems and eventually fails to converge within 1000 Newton-Raphson iterations as early as shown in Figure 4.6(b). The dead end can be marginally protracted by slowing down the insertion velocity or by further reducing the timestep, but high packing densities are still unreachable. It has been observed that serious convergence failure sets in as soon as multiple contacts involving around three to four elements are present, which is intuitively clear given the missing off-diagonal blocks in the Jacobians.
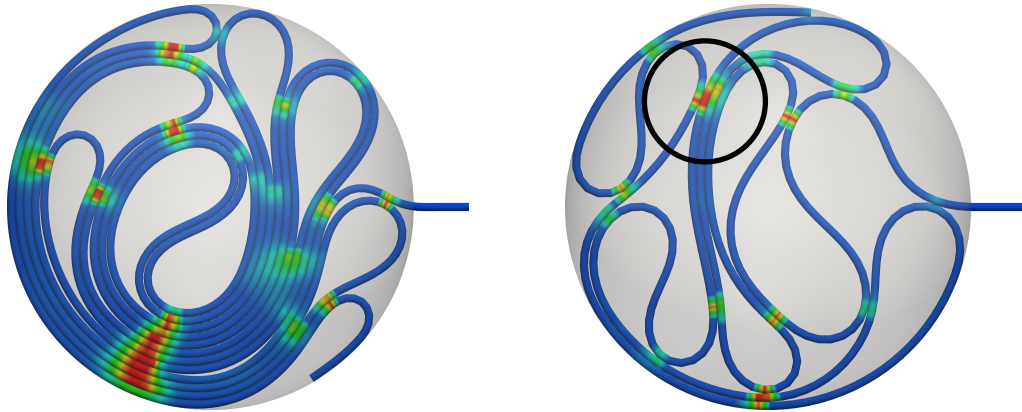
(a) Multiple self-contacts cause no trouble with explicit integration.

(b) Implicit integration. Convergence failure sets in at self-contacts involving three to four elements (black circle).

Figure 4.6.: Convergence failure of the implicit solver in 2D. The color encodes the self-contact energy distribution (blue = 0, red = high). Energies due to cavity contact are not shown.
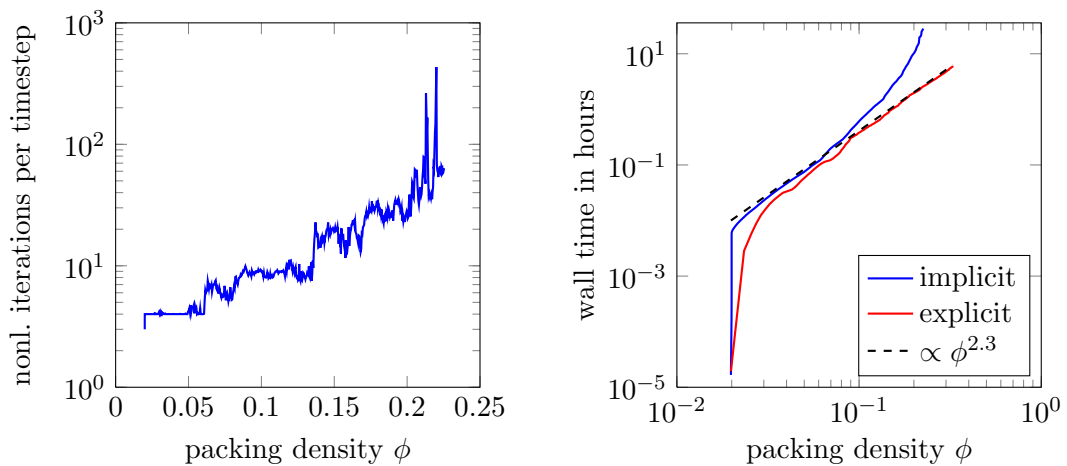
(a) Number of iterations per timestep until convergence of the Newton-Raphson line search. Each data point shows the average over 100 timesteps.

(b) The cumulated wall time in units of hours is plotted against the packing density.

Figure 4.7.: Quantification of convergence failure of the implicit solver based on the example system shown in Figure 4.6.

In Figure 4.7 the problem is quantified more rigorously. Figure 4.7(a) plots the number of nonlinear iterations per timestep required for convergence in the above-mentioned sample setting as a function of the packing density for a single simulation run. The packing density ϕ computes as

$$\phi = \frac{2rL}{\pi ac} \tag{4.9}$$

in 2D, and

$$\phi = \frac{\pi r^2 L}{4/3\,\pi abc} \tag{4.10}$$

in 3D, where $L = \sum_e h_e$ is the "uncompressed" length of the wire inserted into the cavity. If more than 1000 iterations are needed, the iteration is considered diverged. Quite evidently, the number of line search iterations quickly increases to infeasible values. This is also reflected in the total wall time shown in Figure 4.7(b). Long before the dense packing regime is reached, the required simulation time explodes as a consequence of convergence difficulties.

The same convergence problems naturally also appear in 3D. Figure 4.8 shows a simple example of a multi-contact situation where a further advance in implicit integration is blocked by convergence failure.
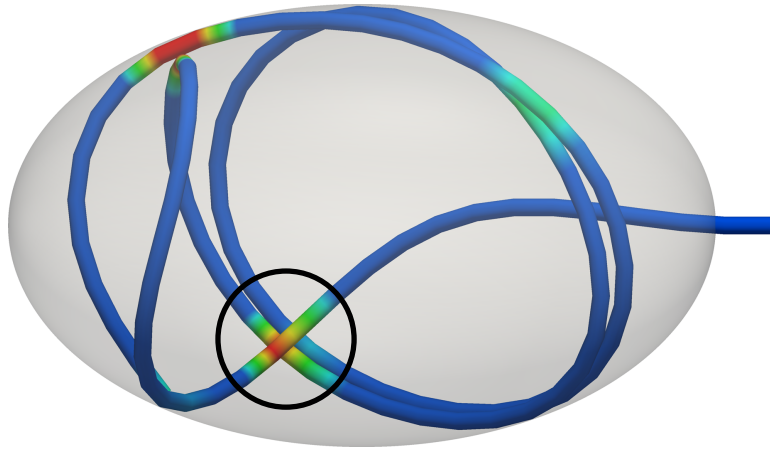

**Figure 4.8.:** Convergence failure of the implicit solver in 3D. Like in two dimensions, the occurance of wire-wire contacts involving about three elements (black circle) causes divergence, effectively inhibiting further progress in the simulation.

Toward the end of Section 2.4 it has been indicated that the corotational transformation makes up a significant fraction of the overall CPU time. This statement is supported by the following data. The relative performance of single program components has been measured using `libMesh`'s built-in event monitoring tool. For the implicit solver, the same example system as above in Figure 4.6(b) is chosen, because the highest packing densities were reached with that one, contrary to three-dimensional setups, for instance. For the implicit scheme a spherical three-dimensional cavity of size $r_{\mathrm{cav}}/r = 10$ with element length $h = 1.5r$ is used as shown in Section 4.4. The fully packed limit $\phi \approx 0.8$ is attained. Figure 4.9 plots the wall time percentages of the most expensive operations for both methods, accumulated from the beginning of the simulation. Note that the *disjoint* times are measured, i.e. in cases where one component is a subroutine of another, the wall time of the subroutine doesn't contribute to that of the calling function. Also note that if a basic component is missing in one of the plots, like e.g. self-contact finding in 2D, it's because the corresponding task contributed less than 5% to the total. To amplify the contribution from self-contact finding, no buffer margin ($\delta = 0$) is used in the linked cell method, which leads to heavy exaggeration of the real time needed to determine the contact pairs. Nevertheless, this part of the program consumes less than 5% of the total wall time in the implicit two-dimensional example. Here, the convergence failure of the implicit solver also looms quantitatively. Soon, the Newton-Raphson line search is dominating the computational costs. Quite remarkably, the construction of the tangent stiffness matrix $\mathbf{K}_\sigma$, which is needed for the implicit scheme, still takes up a large fraction of the overall time. This stands in strong contrast to the explicit 3D example, which clearly profits from not having to construct $\mathbf{K}_\sigma$. Under normal circumstances ($\delta > 0$), the corotational transformation consisting of assembling and applying $\mathbf{F}_e$ and calculating the local DoFs is the most expensive component there.
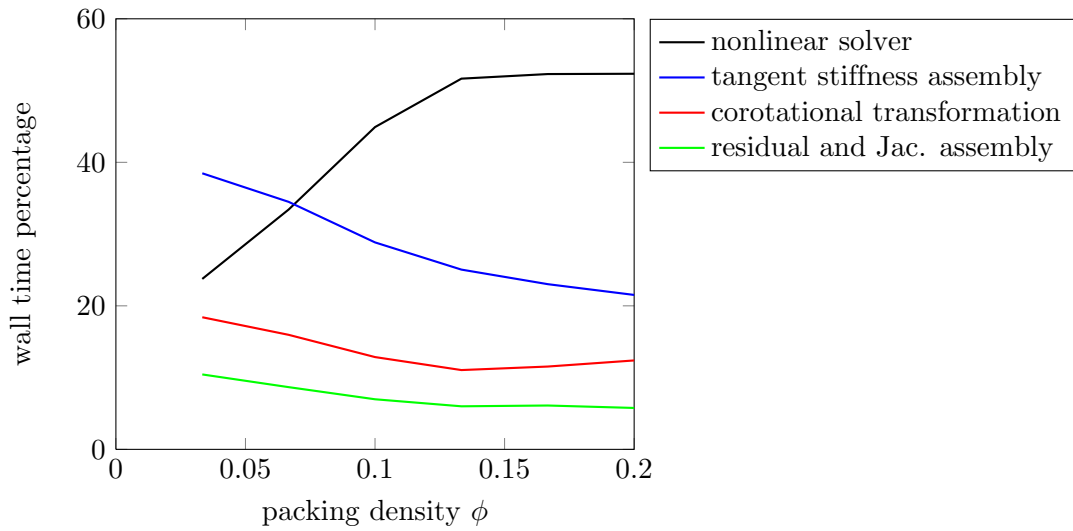
(a) Implicit scheme, 2D
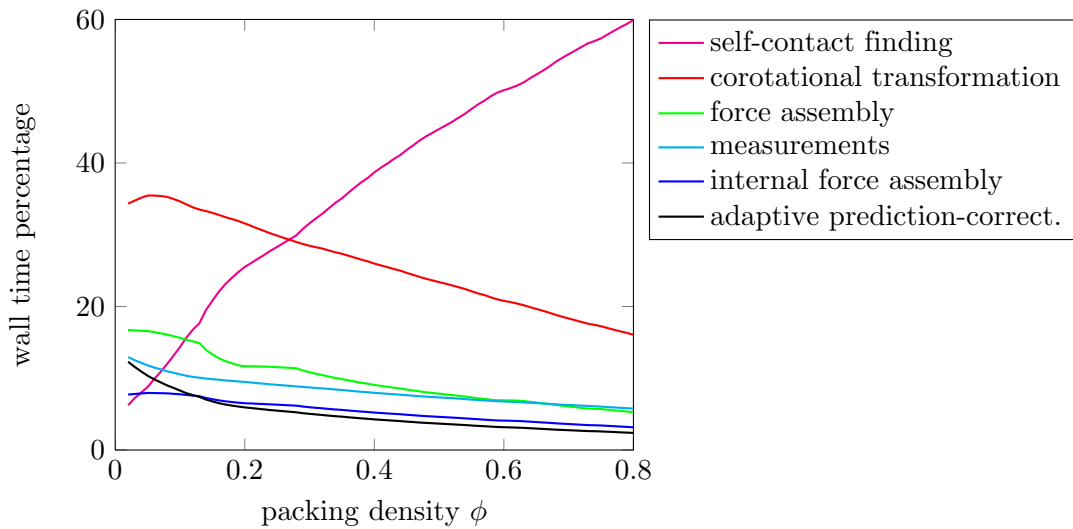
(b) Explicit scheme, 3D

Figure 4.9.: Relative serial performance of program components. The accumulated wall time percentage of the most expensive program components ($> 5\%$) is plotted against the packing density for a single simulation run.

So far, two striking arguments in favor of the explicit predictor-corrector scheme have been given: Ability to cope with multiple self-contacts and performance. Further differences between the two methods that need to be taken into consideration include:

- Even though an implicit scheme may in theory profit from a larger timestep, in practice this is no real advantage, because is has been found that the additional work, resulting from many more iterations per timestep in the Newton-Raphson method when the timestep is increased, is consuming most of the saved time.

- Integrating implicitly requires that the Jacobians for all involved external forces are available. This may or may not be the case in future expansion of the simulation program toward interaction with deformable shells, plasticity or material nonlinearities.

- Breaking the initial axial symmetry of a wire turns out to be much easier when time is integrated explicitly, because the implicit solver quickly smoothens any small random deflection imposed on the wire.

- The explicit scheme cannot handle very stiff wires very well, as the rotational DoFs appear to have a tendency to explode easily. With the implicit solver, no such behavior was encountered.

- Internal wave propagation is more problematic when an explicit method is applied. While with an implicit method *all* nodes are affected immediately when a force is applied on any single node, such interaction propagates only node by node in the explicit method, which results in rather inert waves propagating through the wire. More damping is thus required in practice.

- Parallelizing an implicit method is more involved and requires more interprocess communitation than an explicit one.

- Finally, explicit schemes are usually a lot easier to implement.

For the sum of all these arguments, all subsequent results were obtained with the explicit predictor-corrector method.

4.4. A Spherical Sample System

In this section, basic results for a small spherical cavity in 3D are briefly presented as a proof of concept. The measurement data is also compared to results for the identical system obtained with the discrete element program used in recent studies by Stoop *et al.* [10]. A very small sphere is packed with an intrinsically straight elastic wire at zero friction, entering the sphere in radial direction. The angle of twist at the outermost node is left free, i.e. all torsional energy is allowed to dissipate out of the system. The relevant simulation parameters are $E = 5$, $\rho = 2$, $r_{cav} = 10$, $r = 1$, $h = 1.5$, $c_v = 0.1$. Figure 4.10 shows the resulting densely packed cavity. The observed bending energy nicely coincides for both programs, see Figure 4.11(a). So does the force required to push the wire into the cavity, which is not shown here though. The finite element results (blue) are averaged over 10 simulation runs. In Figure 4.11(b) the number of wire-wire-contacts from the finite element simulations is compared to the number of elements involved in at least one contact from Stoop's discrete elements. The observed small quantitative difference is expected due to the differing measures. The asymptotic behavior follows a power law with an exponent slightly below 2, as theoretically predicted [41] for thick rods $r/r_{cav} \gg 0$.
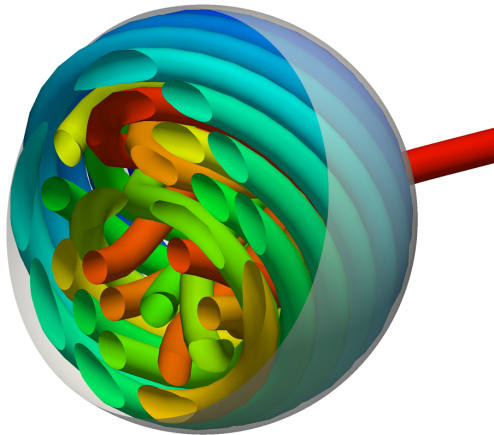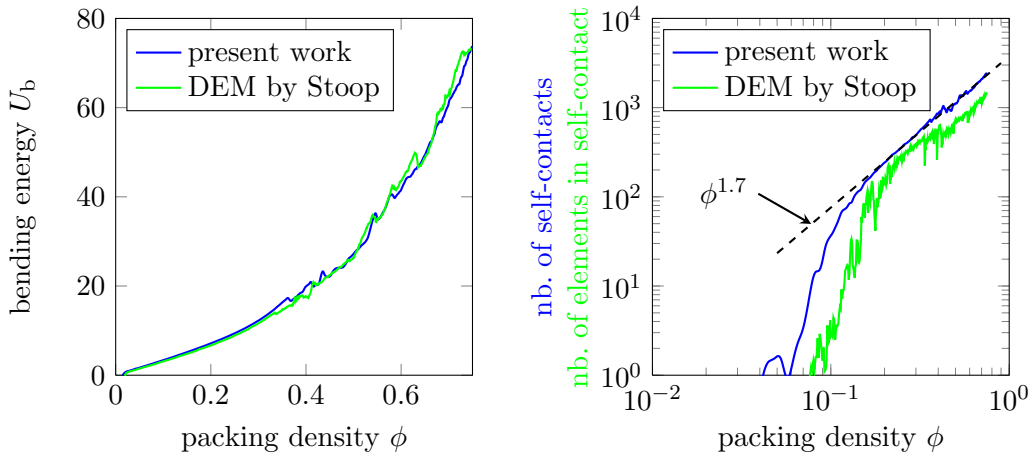

Figure 4.10.: Visualization of the interior of a packed cavity at $\phi = 0.7$. For better visibility, the radius of the wire is reduced to 0.8 and the color encodes the insertion time form early (blue) to late (red).

(a) Comparison of bending energies between the two programs.

(b) The number of self-contact element pairs (e_1, e_2) from the present work is compared to the number of elements contacting at least one other in Stoop's DEM program.

Figure 4.11.: Results for a small spherical sample configuration.

4.5. Breaking the Spherical Symmetry

As a final study in this thesis, the effects of spherical cavity symmetry on the wire morphology is investigated by comparing a few packed ellipsoids to the spherical case. This may be considerd a preliminary step toward deformable biomaterial cavities as they are encountered in saccular aneurysms. So far, previous numerical studies have been limited to the idealized case of exact spherical spatial confinement [8, 10].

Three configurations that are identical except for the cavity aspect ratio in x- and z-direction have been simulated. One of them is spherical with radius $a = b = c = 20r$, the second is an oblate spheroid with radii $a = 10r$, $b = c = 20r$, and the third is a scalene ellipsoid with radii $a = 30r$, $b = 20r$, $c = 10r$. The further simulation settings are $r = 1$, $E = 5$, $\nu = 0.35$, $\rho = 1$, $c_\mathrm{v} = 0.1$, and $v_\mathrm{push} = 0.005$. Figure 4.12 shows the most insightful snapshots from these simulations. Even though the same wires are inserted into these cavities under equal physical conditions, the resulting coiling morphologies are completely distinct. A frictionless elastic wire is highly susceptible to the presence of a preferred orientation given by different curvatures at the interior cavity walls. For instance, coiling in a scalene ellipsoid predominantly happens perpendicular to the shortest semi-principal axis, which leads to open holes in the wire bulk, cf. Figure 4.12(d). This might be relevant to endovascular coiling, where a large fraction of the arterial wall is sought to be covered.

Despite not being shown here, a few prolate spheroids ($a > b = c$) have also been simulated and were found to yield interesting writhing patterns arising from self-contacts together with tight spacial confinement, which will be worth studying more thoroughly.
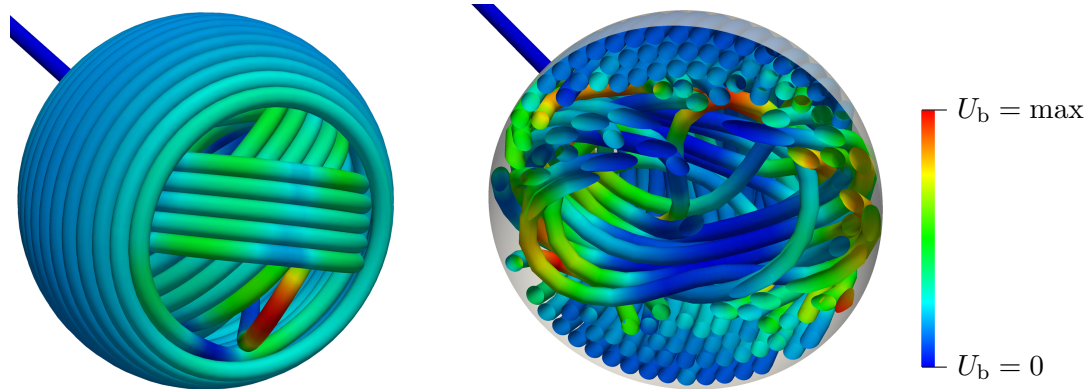
(a) Sphere: $a = b = c = 20r$ at $\phi = 0.35$. The wire coils to form several shells in the outer regions, quickly covering most of the cavity interface.

(b) Cross section of the sphere at $\phi = 0.55$. Tansverse coiling directions support the closure of open gaps (left and right).
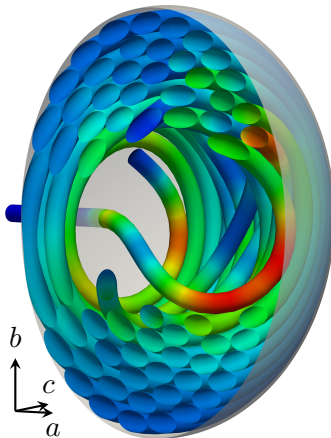
(c) Cross section of an oblate spheroid at $\phi = 0.58$: $a = 10r$, $b = c = 20r$. Very strongly ordered morphology with densely aligned circular coiling at minimum curvature.
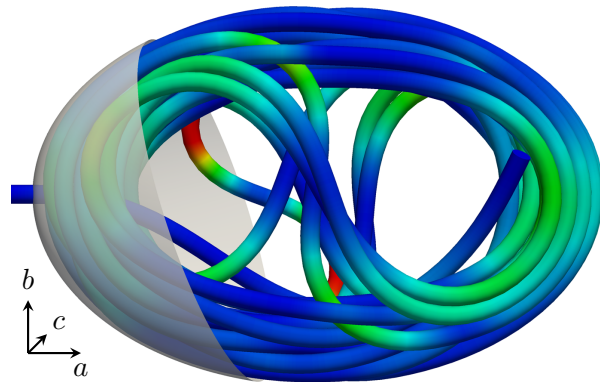
(d) Scalene ellipsoid at $\phi = 0.3$: $a = 30r$, $b = 20r$, $c = 10r$. The wire disorderedly coils along the path of lowest curvature, leaving two gaping holes for very long.

Figure 4.12.: Different coiling structures resulting from different ellispoidal shapes. The bending energy U_b is used for coloring, from zero (blue) to the respective maximum (red).

5. Conclusion & Outlook

In the present thesis a detailed description of a finite element model to simulate the packing of elastic wires in two- and three-dimensional cavities has been given. The program has been implemented with the aid of the `libMesh` and PETSc open-source libraries. Reddy's locking-free simplified third-order beam theory was emplyed to model the bending deflections of the wire. Geometric nonlinearity has been introduced to the theory by means of the corotational formulation provided by Crisfield, assuming large displacements and rotations, but small strains. Interactions of the wire with hard ellipsoidal cavities and wire-wire contacts were carefully included into the finite element model. For efficiency, the popular linked cell lists were implemented for self-contact searching. By comparison to published analyical and numerical results, it has been thoroughly verified that the implementations are faultless.

Two numerical recipes for integrating the hyperbolic equations of motion in time have then been described: The constant-average acceleration method was used as an *implicit* scheme, and an adaptive-timestep predictor-corrector method served as the *explicit* counterpart. For the former, all internal and external forces needed to be supplemented by their Jacobians for the Newton-Raphson iterations. Before late, it was found that the implicit scheme is completely unsuited for the problem of arbitrarily distributed self-contacts as they occur in the packing of rods, the two main reasons being the static sparsity pattern of the Jacobian, and performance. It can safely be concluded that implicit integration in time is not an option in the present case, perhaps unless combined with explicit treatment of self-contacts in a hybrid method. With the explicit solver, few small sample configurations were solved, both spherical and ellipsoidal. The latter is a novel achievement, since published numerical studies concentrate on spherical confinement.

The long-term goal, toward which the present work contributes the first step, is the development of an efficient numerical tool for simulating the dynamic interaction between coiling elasto-plastic wires and ductile cavities of varying shape, including material nonlinearities and friction. To this end, both the wire and a shell-type cavity will be unified in a consistent finite element program. The corotational framework provides a natural setup in which plasticity can easily be added via non-zero intrinsic curvature in (2.34).

Bibliography

[1] G. Guglielmi, F. Viñuela, I. Sepetka, and V. Macellari, Electrothrombosis of saccular aneurysms via endovascular approach. Part 1: Electrochemical basis, technique, and experimental results, J. Neurosurg. **75** (1991) 1–7.

G. Guglielmi, F. Viñuela, J. Dion, and G. Duckwiler, Electrothrombosis of saccular aneurysms via endovascular approach. Part 2: Preliminary clinical experience, J. Neurosurg. **75** (1991) 8–14.

[2] S. Tamatani, Y. Ito, H. Abe, T. Koike, S. Takeuchi, and R. Tanaka, Evaluation of the Stability of Aneurysms after Embolization Using Detachable Coils: Correlation between Stability of Aneurysms and Embolized Volume of Aneurysms, Am. J. Neuroradiol. **23** (2002) 762–767.

[3] C. C. Donato, M. A. F. Gomes, and R. E. de Souza, Crumpled wires in two dimensions, Phys. Rev. E **66** (2002) 015102.

[4] C. C. Donato, M. A. F. Gomes, and R. E. de Souza, Scaling properties in the packing of crumpled wires, Phys. Rev. E **67** (2003) 026110.

[5] C. Donato, F. Oliveira, and M. Gomes, Anomalous diffusion on crumpled wires in two dimensions, Physica A **368** (2006) 1–6.

[6] C. C. Donato and M. A. F. Gomes, Condensation of elastic energy in two-dimensional packing of wires, Phys. Rev. E **75** (2007) 066113.

[7] M. A. F. Gomes, V. P. Brito, A. S. O. Coelho, and C. C. Donato, Plastic deformation of 2D crumpled wires, J. Phys. D: Appl. Phys. **41** (2008) 235408.

[8] N. Stoop, F. K. Wittel, and H. J. Herrmann, Morphological Phases of Crumpled Wire, Phys. Rev. Lett. **101** (2008) 094101.

[9] M. A. F. Gomes, V. P. Brito, and M. S. Araújo, Geometric properties of crumpled wires and the condensed non-solid packing state of very long molecular chains, J. Braz. Chem. Soc. **19** (2008) 293–298.

[10] N. Stoop, J. Najafi, F. K. Wittel, M. Habibi, and H. J. Herrmann, Packing of elastic wires in spherical cavities. *Accepted for publication in Phys. Rev. Lett.* (2011).

[11] N. M. Newmark, A Method of Computation for Structural Dynamics, J. Eng. Mech. Div. **85** (1959) 67–94.

[12] P. Tong, T. H. H. Pian, and L. L. Bucciarblli, Mode shapes and frequencies by finite element method using consistent and lumped masses, Comput. Struct. **1** (1971) 623–638.

[13] C. Felippa, Introduction to Finite Element Methods, 2010. Lecture delivered at University of Colorado, Boulder. `http://www.colorado.edu/engineering/cas/courses.d/IFEM.d/IFEM.Ch32.d/IFEM.Ch32.pdf`.

[14] J. N. Reddy, On locking-free shear deformable beam finite elements, Comput. Methods Appl. Mech. Eng. **149** (1997) 113–132.

[15] S. P. Timoshenko, On the correction for shear of the differential equation for transverse vibrations of prismatic bars, Philos. Mag. **41** (1921) 744–746.

[16] S. P. Timoshenko, On the transverse vibrations of bars of uniform cross-section, Philos. Mag. **43** (1922) 125–131.

[17] A. Tessler and S. Dong, On a hierarchy of conforming Timoshenko beam elements, Comput. Struct. **14** (1981) 335–344.

[18] G. Prathap and G. R. Bhashyam, Reduced integration and the shear-flexible beam element, Int. J. Numer. Methods Eng. **18** (1982) 195–210.

[19] J. N. Reddy, C. M. Wang, and K. Y. Lam, Unified finite elements based on the classical and shear deformation theories of beams and axisymmetric circular plates, Commun. Numer. Methods Eng. **13** (1997) 495–510.

[20] O. C. Zienkiewicz and R. L. Taylor, The Finite Element Method for Solid and Structural Mechanics. Elsevier Butterworth-Heinemann, Oxford, 6th edition, 2005. ISBN 0-7506-6321-9.

[21] A. A. Shabana, Computational Continuum Mechanics. Cambridge University Press, 2008. ISBN 0-521-88569-8.

[22] K. Mattiasson, A. Bengtsson, and A. Samuelsson, On the accuracy and efficiency of numerical algorithms for geometrically nonlinear structural analysis, in *Finite Element Methods for Nonlinear Problems*, P. G. Bergan, K. J. Bathe, and W. Wunderlich, eds., pp. 3–23. Springer Verlag Berlin, Heidelberg, 1986. ISBN 3-540-16226-7.

[23] Y. Urthaler and J. N. Reddy, A corotational finite element formulation for the analysis of planar beams, Commun. Numer. Methods Eng. **21** (2005) 553–570.

[24] T. Belytschko and B. J. Hsieh, Non-linear transient finite element analysis with convected co-ordinates, Int. J. Numer. Methods Eng. **7** (1973) 255–271.

[25] C. C. Rankin and F. A. Brogan, An Element Independent Corotational Procedure for the Treatment of Large Rotations, J. Press. Vessel Technol. **108** (1986) 165–174.

[26] L. H. Teh and M. J. Clarke, Co-rotational and Lagrangian formulations for elastic three-dimensional beam finite elements, J. Construct. Steel Res. **48** (1998) 123–144.

[27] M. A. Crisfield, A consistent co-rotational formulation for non-linear, three-dimensional, beam-elements, Comput. Methods Appl. Mech. Eng. **81** (1990) 131–150.

[28] G. Wempner, Finite elements, finite rotations and small strains of flexible shells, Int. J. Solids Struct. **5** (1969) 117–153.

[29] C. Oran, Tangent Stiffness in Plane Frames, J. Struct. Div. **99** (1973) 973–985.
C. Oran, Tangent Stiffness in Space Frames, J. Struct. Div. **99** (1973) 987–1001.

[30] M. A. Crisfield, Non-linear Finite Element Analysis of Solids and Structures: Volume 1: Essentials. John Wiley & Sons, Chichester, 1996. ISBN 0-471-97059-X.
M. A. Crisfield, Non-linear Finite Element Analysis of Solids and Structures: Volume 2: Advanced Topics. John Wiley & Sons, Chichester, 1997. ISBN 0-471-95649-X.

[31] J. N. Reddy, Nonlocal theories for bending, buckling and vibration of beams, Int. J. Eng. Sci. **45** (2007) 288–307.

[32] H. R. Hertz, Über die Berührung fester elastischer Körper, J. Reine Angew. Math. **92** (1882) 156–171.

[33] K. L. Johnson, Contact Mechanics. Cambridge University Press, Cambridge, 1985. ISBN 0-521-34796-3.

[34] J. C. Hart, Distance to an Ellipsoid, in *Graphics Gems IV*, P. S. Heckbert, ed., pp. 113–119. Academic Press, 1994. ISBN 0-12-336155-9.

[35] K. Thomsen, Surface Area of an Ellipsoid, 2004. http://www.numericana.com/answer/ellipsoid.htm#thomsen.

[36] B. S. Kirk, J. W. Peterson, R. H. Stogner, and G. F. Carey, `libMesh`: a C++ library for parallel adaptive mesh refinement/coarsening simulations, Eng. Comput. **22** (2006) 237–254.

[37] S. Balay, W. D. Gropp, L. C. McInnes, and B. F. Smith, Efficient Management of Parallelism in Object Oriented Numerical Software Libraries, in *Modern Software Tools for Scientific Computing*, E. Arge, A. M. Bruaset, and H. P. Langtangen, eds., pp. 163–202. Birkhäuser Press, Cambridge, 1997. ISBN 0-8176-3974-8.

[38] L. F. Zeng, N.-E. Wiberg, X. D. Li, and Y. M. Xie, *A posteriori* local error estimation and adaptive time-stepping for Newmark integration in dynamic analysis, Earthquake Engng Struct. Dyn. **21** (1992) 555–571.

[39] J. N. Reddy, An Introduction to Nonlinear Finite Element Analysis. Oxford University Press, Oxford, 2004. ISBN 0-19-852529-X.

[40] O. C. Zienkiewicz and Y. M. Xie, A simple error estimator and adaptive time stepping procedure for dynamic analysis, Earthquake Engng Struct. Dyn. **20** (1991) 871–887.

[41] A. P. Philipse, The Random Contact Equation and Its Implications for (Colloidal) Rods in Packings, Suspensions, and Anisotropic Powders, Langmuir **12** (1996) 1127–1133.

[42] D. Sunday, Distance between Lines and Segments with their Closest Point of Approach, 2001. http://www.softsurfer.com/Archive/algorithm_0106/algorithm_0106.htm.

[43] D. Eberly, Distance Between Two Line Segments in 3D, 1999.
http://www.geometrictools.com/Documentation/DistanceLine3Line3.pdf.

D. Eberly, 3D Game Engine Design: A Practical Approach to Real-Time
Computer Graphics. Morgan Kaufmann, 2000. ISBN 1-55860-593-2.

[44] B. Quentrec and C. Brot, New Method for Searching for Neighbors in Molecular
Dynamics Computations, J. Comput. Phys. **13** (1973) 430–432.

[45] K.-J. Bathe and S. Bolourchi, Large displacement analysis of three-dimensional
beam structures, Int. J. Numer. Methods Engrg. **14** (1979) 961–986.

[46] J. C. Simo and L. Vu-Quoc, A three-dimensional finite-strain rod model. Part II:
Computational aspects, Comput. Methods Appl. Mech. Eng. **58** (1986) 79–116.

[47] A. Cardona and M. Geradin, A beam finite element non-linear theory with finite
rotations, Int. J. Numer. Methods Eng. **26** (1988) 2403–2438.

[48] W. Schnell, D. Gross, and W. Hauger, Technische Mechanik 2: Elastostatik.
Springer, Berlin, 5th edition, 1995. ISBN 3-540-58696-2.

A. DVD Contents

Along with this work comes a DVD containing the following folders and data:

Folder or file name	Contents
`data`	Raw input and output data from various selected simulations in 2D and 3D.
`report`	The present thesis in PDF format and the LaTeX sourcecode including all figures.
`src`	All C++ source files, the makefile, and a sample configuration file.
`videos`	Five DivX-encoded video files showing wire insertions into various two- and three-dimensional cavities.
`readme.txt`	Informations about compiling `libMesh` and PETSc, running the program, and a TODO list.